

UNIVERSITY OF CALIFORNIA
Santa Barbara

Frequency Division Using A Micromechanical
Resonance Cascade

A Dissertation submitted in partial satisfaction
of the requirements for the degree of

Doctor of Philosophy

in

Mechanical Engineering

by

Kamala R. Qalandar

Committee in Charge:

Professor Kimberly L. Turner, Chair

Professor Carl Meinhart

Professor Matthew Begley

Professor Ania Jayich

March 2017

The Dissertation of
Kamala R. Qalandar is approved:

Professor Carl Meinhart

Professor Matthew Begley

Professor Ania Jayich

Professor Kimberly L. Turner, Committee Chairperson

December 2016

Frequency Division Using A Micromechanical Resonance Cascade

Copyright © 2017

by

Kamala R. Qalandar

To my children.

Acknowledgements

There are simply not enough pages for me to acknowledge everyone who has helped me on this journey. To everyone I crossed paths with in the academic world, know that I appreciate all of your knowledge and wisdom. To all of my friends who asked how my research was going, and to everyone in my family who listened to my practice talks and helped me proofread, thank you.

I'd first like to acknowledge the support, guidance, and advice of my advisor, Professor Kimberly Turner. Since joining this research group, I have grown as a researcher, educator, and leader, and I'd like to thank her for giving me the freedom to work on the most interesting problems while also pushing me to overcome the most difficult obstacles. I'd also like to thank the other members of my committee, Professors Carl Meinhart, Matthew Begley, and Ania Jayich for their excellent questions and valuable input. I'm also very grateful to Professor Steven Shaw at Michigan State University, who has always been exceedingly generous with his time and feedback.

Thank you also to TMEMS students past and present for being brilliant and dedicated colleagues, with particular thanks to Dr. Kari Moran, who gives a good pep talk and an even better tutorial on how to derive nonlinear stiffness terms; to Brian Gibson, who can design a test set-up for anything and spent many hours talking through the details of the many projects we've shared over the last four

years; and to Lily Li, a gifted researcher and great friend with whom I've enjoyed discussing the details of theory, experiments, and the necessity of coffee.

I also want to acknowledge my UCSB-based support team. Thank you to Professor Glenn Beltz, who gave me a second chance at college when he had no earthly reason to do so, and who supported me every step of the way for the next eight years through my undergraduate and graduate years; I'd like to thank him and Professor Danielle Swiontek for their guidance and advice on life, academia, and my future. And to Suzi See, who opened her office to me in times of need and triumph, and who inspired me to write this document in the first place - thank you; your impact on my life cannot be measured.

Thanks, of course, to my two beautiful children, who are the reason I returned to school in the first place, and to Sonya, Jake, and Issa for helping us take care of them.

And lastly, thank you to my husband, whose unwavering support and infinite calmness are things of wonder.

Curriculum Vitæ

Kamala R. Qalandar

Education

- 2016 Doctor of Philosophy in Mechanical Engineering, University of California Santa Barbara.
- 2009 Bachelor of Science in Mechanical Engineering, University of California Santa Barbara.

Professional Experience

- 2009 – 2016 Graduate Research Assistant, Mechanics of Microscale Systems Lab, University of California Santa Barbara
- 2009 – 2015 Graduate Teaching Assistant for Mechanical Engineering Design and Capstone Courses, Department of Mechanical Engineering, University of California Santa Barbara
- 2014 – 2016 Member, Undergraduate Advisory Committee, Department of Mechanical Engineering, University of California Santa Barbara
- 2013, 2015, 2016 Lecturer, Department of Mechanical Engineering, University of California Santa Barbara

Selected Publications

B. Gibson, K.R. Qalandar, G. Piazza, and K.L. Turner: “A Novel Method for Measuring Ring-Down In a High Noise And High Frequency System Using Laser Doppler Vibrometry,” In *Proceedings of Solid State Sensors, Actuators, and Microsystems Workshop*, Hilton Head SC, June 2016.

B. Gibson, K.R. Qalandar, C. Cassella, G. Piazza, and K.L. Turner: “Analysis of the impact of release area on the quality factor of contour-mode resonators by laser Doppler Vibrometry,” In *Frequency Control Symposium and the European Frequency and Time Forum, Joint Conference of IEEE International*, 2015.

K.R. Qalandar, B.S. Strachan, B. Gibson, M. Sharma, A. Ma, S.W. Shaw, and K.L. Turner: “Frequency division using a micromechanical resonance cascade,” In *Applied Physics Letters*, December 2014.

B.S. Strachan, K.R. Qalandar, B. Gibson, M. Sharma, P. Polunin, S.W. Shaw, K.L. Turner, “A passive micromechanical frequency divider,” In *Proceedings of Solid State Sensors, Actuators, and Microsystems Workshop* Hilton Head SC, June 2014.

E.J. Ng, Y. Yang, V.A. Hong, C.H. Ahn, D.L. Christensen, B. Gibson, K.R. Qalandar, K.L. Turner, T.W. Kenny, “Stable pull-in electrodes for narrow gap actuation,” In *Proceedings of IEEE MEMS 2014*, MEMS 2014.

K.R. Qalandar, B. Gibson, L. Shaw, S. Chiu, A. Tazzoli, J. Segovia, M. Rinaldi, G. Piazza, K.L. Turner, “Finite element modeling verification of high frequency piezoelectric contour-mode MEMS resonators using laser vibrometry,” In *AVS-60*, Laguna Beach CA 2013.

Abstract

Frequency Division Using A Micromechanical Resonance Cascade

Kamala R. Qalandar

Frequency conversion mechanisms are essential elements in frequency synthesizers, which are used in many applications ranging from microwave and RF transceivers to wireless applications to vibration energy harvesters. In particular, the frequency divider, which is an integral part of the phase-locked loop circuit, is essential in modern day instrumentation and wireless communications. In most systems requiring frequency conversion, electronic frequency converters are used; these components require significant power input and introduce noise into the system. In this dissertation, we introduce a mechanism for eliminating these noisy electronic components by using coupled mechanical elements. This novel mechanism for frequency division using parametric resonance in MEMS relies on finite deformation kinematics and nonlinear coupling between isolated modes in a structure to divide an input signal through multiple stages using purely mechanical coupling.

We present the theoretical framework for a generic subharmonic resonance cascade. Design considerations for one specific implementation are discussed, and

a proof-of-concept for low-noise low-power applications is demonstrated. A single input signal is divided through three modal stages, generating output signals at $\frac{1}{2}$, $\frac{1}{4}$, and $\frac{1}{8}$ of the input signal. Coupling and boundary conditions are explored, as well as the noise characteristics of this mechanical frequency divider. We show that this type of cascading frequency conversion improves phase noise performance of each individual mode.

Professor Kimberly L. Turner
Dissertation Committee Chair

Contents

Acknowledgements	v
Curriculum Vitæ	vii
Abstract	x
List of Figures	xiv
List of Tables	xvi
1 Introduction	1
2 Background	4
2.1 Frequency Conversion and Coupled Systems	4
2.2 Resonance Phenomena	9
2.2.1 Linear and Nonlinear Resonance	9
2.2.2 Parametric Resonance	14
3 Mechanical Divider Theory and Design	23
3.1 Subharmonic resonance cascade theory	23
3.2 Modeling of Coupled Modes	25
3.2.1 Coupled Modes: Long Chain	25
3.2.2 Two Coupled Modes	28
3.3 Semicircular Spring Implementation	32
3.3.1 Design Considerations	32
3.3.2 Numerical Analysis - Modal Mechanics	35
3.3.3 Finite Element Modeling	40

4	Experimental Cascade	43
4.1	Fabrication	43
4.2	Experimental Results: Divide-by-eight Cascade	44
4.3	Device Characterization: Two Coupled Modes	53
5	Noise In A Resonance Cascade	61
5.1	Noise in MEMS	61
5.1.1	Measuring Phase Noise	64
5.1.2	Reducing Phase Noise	67
5.2	Phase noise in a cascade	71
6	Future Work	81
6.1	Improving Performance	81
6.2	Device Design	82
6.3	Characterization	84
	Bibliography	88
	Appendices	97
A	Beam-Spring Stiffness	98

List of Figures

2.1	Representative amplitude-frequency response of a harmonic oscillator subjected to increasing forcing strength.	11
2.2	Amplitude frequency response curves for system with Duffing non-linearity	13
2.3	Schematic of wedge of instability for a micromechanical system. . .	18
2.4	Parametric resonance in an axially-forced beam.	20
2.5	Stable and unstable solutions for primary parametric resonance instability region.	21
2.6	Response of a doubly-clamped beam subjected to axial loading . .	22
3.1	Generic model of a mechanical subharmonic resonance cascade . .	24
3.2	Full activation of a seven-stage cascade.	28
3.3	Response of a fully actuated seven-stage cascade	29
3.4	Two coupled mode: forcing	30
3.5	Two coupled modes: nonlinear damping	32
3.6	Three implementations of orthogonal microbeam frequency dividers	33
3.7	Design dimensions for a mechanical frequency divider	36
3.8	Mechanics and geometry.	39
3.9	Modal analysis of three-stage frequency divider	42
4.1	SEM micrograph of mechanical frequency divider	45
4.2	Parametric resonance zones for modes 2, 3 and 4 of the device . .	48
4.3	Normalized instability regions	49
4.4	Cascaded parametric response	51
4.5	Measured amplitudes from modes 2-4	52
4.6	Experimental setup using external components.	54
4.7	Individual tongues for modes 2-4	55
4.8	Linear response of mode 2 and mode 3	56

4.9	Two response peaks in mode 3	57
4.10	Individual instability regions after post-processing	58
4.11	Cascade actuation.	60
5.1	Experimental setup for measuring phase noise.	67
5.2	Noise characteristics of modes 2 and 3 at resonance.	74
5.3	Noise in a two-stage cascade	75
5.4	Frequency response of modes 2 and 3 at varying pressure.	78
5.5	Noise in a subharmonic resonance cascade	80
A.1	Free body diagram of single beam-spring	98

List of Tables

3.1 Comparison of analytical and finite elements methods for determining stiffness	37
4.1 Device design parameters.	47
6.1 Array dimensions	85

Chapter 1

Introduction

Microelectromechanical systems (MEMS) are systems that combine electrical and mechanical components, created using microfabrication techniques, to create new technology at the microscale. Though there's some disagreement on when the field of MEMS was first established, or whether Richard Feynman's 1952 lecture *There's Plenty of Room at the Bottom* [1] was really as influential as it appears in hindsight, we can all agree that some of the most significant "firsts" in the field occurred in the 1960's and 1970's - the evolution of surface micromachining techniques, the development of capacitive pressure sensors, and the invention of microprocessors are just a few of many examples [2, 3]. Then, Kurt Peterson's 1982 paper *Silicon as a Mechanical Material* [4] laid the groundwork for future structural MEMS design by describing methods of fabrication for many types of silicon MEMS devices, and shortly thereafter, in 1986, the term "microelectromechanical system" was first introduced. Since these early days, the field of MEMS

has expanded to include a wide range of areas of interest, including subjects as varied as microfluidics, bio-mems, point-of-care medical systems, and energy harvesters.

As microfabrication techniques are refined, smaller length scales and higher frequencies can be repeatably realized. In the field of resonant MEMS, as frequency goes up and size goes down, significant concerns that already exist - phase noise, power consumption, and anchor loss are just a few examples - become even more significant. The accuracy of the frequency reference itself can be the limiting factor in determining what practical applications a particular technology has [5], and low quality factor electronic elements can also add noise to a system [6], even when the system uses a frequency reference with good noise characteristics.

Frequency synthesizers, which are used in many applications ranging from microwave and RF transceivers to wireless applications to vibration energy harvesters [7, 8, 9, 10], have a high power consumption because of the electronic elements, rather than the frequency setting element. In this dissertation, we introduce a mechanism for eliminating these noisy electronic components by using coupled mechanical elements. This novel mechanism for frequency division using parametric resonance in MEMS relies on finite deformation kinematics and non-linear coupling between isolated modes in a structure to divide an input signal through multiple stages using purely mechanical coupling [11, 12]. We demon-

strate successful divide-by-eight operation, and show that this type of cascading frequency conversion improves phase noise performance of each individual mode.

Chapter 2 gives an introduction to parametric resonance and discusses examples of coupled resonators in current literature. In Chapter 3, the theoretical framework for a generic subharmonic resonance cascade is presented, and design considerations for one specific implementation are discussed. In Chapter 4, a proof-of-concept for low-noise low-power applications is demonstrated, and the coupling and boundary conditions are explored. Chapter 5 discusses the precision and accuracy of these dividers. Finally, in Chapter 6, we discuss other types of mechanical frequency dividers to be fabricated and tested in the future, as well as other drive and sense mechanisms. We also investigate the possibility of tuning the coupling strength of such systems using finite element modeling. The conclusion of this work is that nonlinearity in MEMS is not something to fear - not only are nonlinearities unavoidable, they can be utilized in novel design or for better performance. Using parametric resonance and nonlinear intermodal coupling, we demonstrate mechanical frequency division with improved noise characteristics over traditional operation.

Chapter 2

Background

2.1 Frequency Conversion and Coupled Systems

Frequency conversion mechanisms are essential elements in frequency synthesizers [13, 7]. Frequency synthesizers, which generate a range of signals from a single stable input signal, are used in many applications, ranging from microwave and RF transceivers to wireless applications to vibration energy harvesters [7, 8, 9, 10]. In particular, the frequency divider, which is an integral part of the phase-locked loop circuit, is essential in modern day instrumentation and wireless communications. The design of the frequency divider is critical as it is generally the element in the circuit that requires the most power, and significant literature exists covering the research on low power frequency dividers [14, 15]. Accuracy and precision in these frequency conversion mechanisms are essential, particularly in wireless technology, which relies on precise selection of a signal on a particular channel.

With small frequency bands near each other on the spectrum, small unintended frequency shifts can lead to the problem of crossed signals, which highlights the need to limit phase noise in frequency conversion mechanisms.

In most systems requiring frequency conversion, electronic frequency converters are used [13, 6]. Solid-state devices have dominated this field due to wide bandwidth operation and ease of implementation. In [13], two types of GaAs-based frequency dividers with divide-by-two operation are presented: a parametric divider and a regenerative type divider, which can generally operate over a wider range of frequencies and drive levels. Regenerative dividers, also referred to as Miller dividers, can be used to divide a signal by $N+1$ where N is an integer, and generally show better phase noise characteristics than traditional digital dividers [16]. Fractional- N dividers, seen in [17] and [18], use a time-average of two dividers to select a particular frequency. [19] demonstrates a cascading CMOS divider at 40 GHz with an input range of 2.3 GHz, with two successive divide-by-two stages. There are several demonstrations of cascading conversion stages, but they generally require amplifiers and buffers for cascading conversion stages [13, 19, 20] and preventing back-coupling [21, 22]. Input phase noise variations in a phase-locked loop are multiplied by N at the output, so a frequency divider actually increases noise by $20 \log(N)$ [6]. This noise can be high enough to mask noise floor of input oscillator. In single-stage conversion mechanisms, such as prescalers or fractional-

N synthesizers, or cascading converters with successive division stages, the active elements are the main sources of noise.

Passive dividers are another type of device used for frequency conversion; in this context, passive refers to a mechanism that does not require active elements for dividing frequency and preventing back-coupling, and instead relies on coupled mechanical components. Because passive dividers don't require active elements for operation, they require less power and can avoid the added noise generated by active elements in a circuit. Each output frequency is based on the resonance of a mechanical element; precise design is required for alignment of these resonant modes.

So far, passive frequency dividers, which have the capacity for low phase noise and low power consumption, have only successfully been demonstrated in a single divide-by-two conversion stage [23, 24]. In [23], a capacitive-gap transduced micromechanical array demonstrates single divide-by-two frequency operation through the use of a parametric oscillation effect. This frequency divider requires no active elements, thus adding no additional noise sources outside of that from the frequency source itself. The coupled modes demonstrated frequency division from 121 MHz to 60.6 MHz, with a 23 dB decrease in far-from-carrier noise, which is a significant improvement over the expected 6 dB drop in a divide-by-two

operation (discussed further in Chapter 5). This is attributed to the high quality factor of the device combined with the lack of active elements.

A detailed model of coupled modes in a single resonator structure in autoparametric resonance is presented in [25]. In this work, the response of two modes of an electrostatically-actuated device, with a frequency ratio of 2:1, are simulated. It is shown that with proper choice of drive amplitude, the bandwidth over which the lower frequency mode is actuated can be narrowed, resulting in high quality factor operation. This paper is followed by [26], in which experimental results for a pedal microresonator are presented. A single divide-by-two stage in this microresonator takes advantage of nonlinear coupling between modes: a flexural mode is driven directly, and then quadratic intermodal coupling excites a lower frequency torsional mode, aligned at a 2:1 ratio. This work explores the sensitivity to mistuning of the 2:1 modal frequency ratios, as well as the effects of damping and structural features that alter the targeted design specifications, and demonstrates some of the limitations of frequency conversion with a mechanical frequency divider based on autoparametric resonance. Nayfeh, Asrar, and Nayfeh [27] investigate a system with three internal modes. This study is motivated by internal resonance between modes in a plane; energy in one mode is transferred to a lower frequency mode, inducing vibrations that caused the plane to break apart. In this case, the modes align with 2:1 frequency ratios, and parametric

resonance between the modes causes large amplitude vibrations. In [24], a passive CMOS frequency divider relying on parametric oscillation is presented. It shows a better phase noise performance than a traditional injection-locked divider due to the absence of active elements. This divider also has no static power consumption, which is advantageous for implementation in a phase-locked loop. These types of parametric dividers are capable of producing a larger power output and demonstrating superior phase noise performance to more traditional dividers, but so far have not been shown capable of cascading conversion stages.

There are also cases in literature of parametric excitation of similar resonators, with one frequency division stage occurring between the input signal and the single output signal. In [28], globally coupled oscillators of the same frequency subjected to parametric resonance are studied for the purpose of improved performance and amplified response signal. [29] discusses coupling between 2, 3, and N resonators in a weakly coupled oscillator network. The linearly coupled non-autonomous oscillators synchronize under parametric 2:1 excitation.

A novel frequency conversion method is proposed in [11] that combines the cascading capability demonstrated by solid-state dividers and the passivity of a parametric divider into a single mechanical device. The operation is based on nonlinear dynamics and exploits the robustness of parametric resonance. This method uses a subharmonic resonance cascade in a chain of resonators with ap-

proximate 2:1 natural frequency ratios, with weak nonlinear coupling between the elements that allows energy exchange between them. Of interest is a particular type of this type of system, where the high frequency end of the chain is excited, and the coupling between the elements activates each resonator down the chain. The following chapters cover the modeling, design, and experimental results of such a system.

2.2 Resonance Phenomena

2.2.1 Linear and Nonlinear Resonance

Mechanical resonance can be described as the tendency of a system to oscillate at a greater amplitude at some frequencies than at others. These frequencies are called the resonance frequencies and depend on geometric and material parameters of the system. When the system is driven at or very near one of these resonance frequencies, the amplitude of the response increases, which increases the signal to noise ratio and improves the ability to measure the response.

In mechanics, resonance is described using a mass-spring-damper system. The equation of motion of such a system when it is subjected to sinusoidal external forcing is given by

$$m\ddot{x} + c\dot{x} + kx = F_0\cos(\omega t) \quad (2.1)$$

where m is the mass, c is the damping coefficient, k is the stiffness of the spring, and F_0 and ω are the strength and frequency of the forcing. Resonant motion occurs when ω is very near the resonance frequency. For small values of damping, ω_0 of the forced system is very near the natural frequency of the system, which is given by $\omega_0 = \sqrt{k/m}$, where ω_0 describes the frequency of unforced vibrations. The solution for the sinusoidally-forced resonator is given by $x(t) = A \sin(\omega_0 t + \theta)$ where A is the amplitude and θ refers to the phase of the solution. Note from this solution that the amplitude and frequency of the solution are independent. Ignoring the effects of damping momentarily, with increasing forcing strength, the amplitude of the harmonic response increases linearly (Figure 2.1). As the mass displaces farther from equilibrium, the restoring force pulls back with a force proportional to the displacement, and the period of oscillation remains unchanged.

Nonlinear resonance can be described very simply as the occurrence of resonance in a nonlinear system. Nonlinearities in a MEMS system can arise from various sources, including material properties, boundary conditions, actuation and detection mechanisms, and nonlinear damping [30, 31, 32], and always exist, though they are generally ignored for the sake of simple analysis. Though this approximation of linearity is valid for certain ranges of operation, it also masks

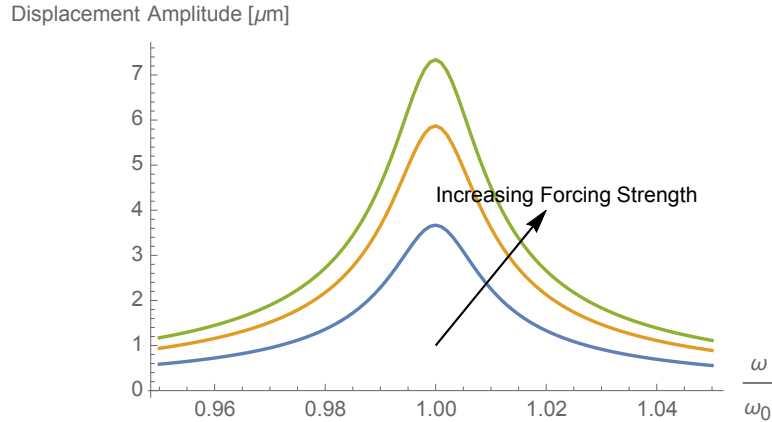


Figure 2.1: Representative amplitude-frequency response of a harmonic oscillator subjected to increasing forcing strength. The x-axis shows ω/ω_0 , where ω is the drive frequency and ω_0 is the resonance frequency. In the linear regime, the resonance frequency is independent of the response amplitude. Increased forcing strength increases the response amplitude, but does not cause a shift in resonance frequency.

the interesting and sometimes useful dynamical properties that arise from the nonlinearities.

In contrast to linear resonance, nonlinear resonance is a phenomenon in which the resonance frequency *does* depend on the amplitude of vibration. The nonlinear restoring force, which can be represented generally by $F = k_1x + k_2x^2 + k_3x^3 + (h.o.t.)$, now means that the eigenfrequency is amplitude dependent. The nonlinear resonance shift is then given by $\omega = \omega_o + \kappa x^2$, where κ is a constant derived from the nonlinear coefficients and x is the amplitude of the displacement.

The Duffing equation [33] is a well-studied example of an equation of motion describing nonlinear resonance [34, 35]. It is used here as an illustrative example

as the cubic nonlinearity it contains describes the dynamics of a doubly-clamped beam resonating at large amplitude, which will be encountered in later chapters. Here, the nonlinear restoring force arises from the axial stretching of the beam. The forced Duffing equation with damping takes the form of

$$m\ddot{x} + c\dot{x} + k_1x + k_3x^3 = F_0\cos(\omega t) \quad (2.2)$$

where m , c , and ω_0 retain the previous definitions, k_1 is the linear stiffness previously defined simply as k , and we introduce k_3 as the coefficient of the cubic stiffness term. If k_3 is positive, κ is positive. Increased forcing increases the amplitude, and the resonance frequency increases; this is known as a hardening nonlinearity. Conversely, if k_3 is negative, increased forcing and amplitude lead to a lower resonance frequency. This is known as a softening nonlinearity. Representative amplitude-frequency curves for both hardening and softening systems are shown in Figure 2.2. Nonlinear systems exhibit the “foldover effect,” demonstrated for positive (left) and negative (right) values of k_3 . For certain values of drive frequency, there is more than one possible solution; in these regions, there are two stable solutions (solid lines) and one unstable solution (dotted line). While the unstable solution is never seen in experiment, the nature of the resonance curve can change depending on which direction the frequency is swept.

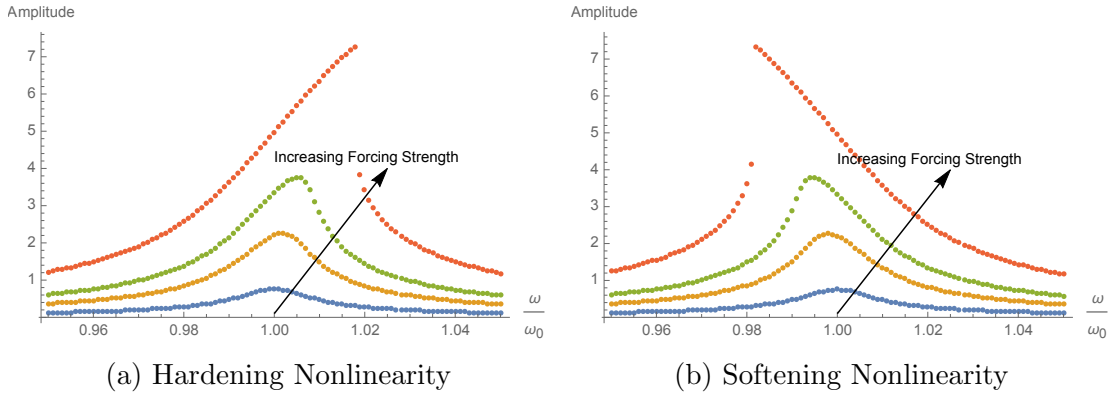


Figure 2.2: Representative amplitude-frequency response curves for system with Duffing nonlinearity. Note that in nonlinear resonance, the resonance frequency is not independent of the response amplitude. Increased forcing strength increases the response amplitude and also causes a frequency shift. Stable solutions are indicated by solid lines, and unstable solutions are indicated by dotted lines.

While analysis of the dynamics of a system generally starts with the assumption of linearity, and almost all design is done in such a way as to increase the range of linear operation, most physical systems possess some degree of nonlinearity. Understanding the sources of nonlinearity, and methods for designing around them, is important. More importantly, nonlinearity in MEMS can be exploited, to increase the dynamic range and improve sensitivity [36, 37, 38]. Ideas for exploiting nonlinearity for improved performance are discussed further in Section 5.1.2.

2.2.2 Parametric Resonance

Parametric resonance is a resonance phenomenon that differs from the previously described linear and nonlinear resonance because it exhibits the instability phenomenon - solutions change from stable to unstable, and vice versa, across instability boundaries that are determined by parameters of the system and the excitation to which it is subjected.

Two classic examples of parametric resonance are the child on a swing [39], where a child sits and stands while swinging, thereby periodically modulating the effective length of the swing and increasing the amplitude of oscillation, and the vertically-forced pendulum [40], where the vertical forcing of the support at twice the natural frequency of the pendulum causes a large amplitude swing of the pendulum. Other examples of physical phenomena described by the Mathieu equation include roll resonance of a ship on water [41], reheating of the universe after inflation [42], analysis of the dynamics of cables in large stayed bridges [43], and oscillations of spherical bubbles in water [44]. The common attribute among these examples concerns the relationship between the frequency of the input and output: an important property of parametric resonance is that in contrast to linear or nonlinear resonance, in which a small excitation near the resonance frequency can produce a large response at that frequency, in parametric excitation, a small

excitation at a frequency far from the natural frequency can produce a large amplitude response at the natural frequency.

This phenomenon arises when a parameter of the system is varied periodically in time at certain frequencies. In this work, we focus on systems with sinusoidally varying stiffness, though the same effect can be achieved when other energy-storage terms are varied in time. In contrast to linear and nonlinear resonance, where external forcing provides the energy to increase the response amplitude, in the examples of parametric resonance covered here, the energy from the external forces varies the stiffness, which acts as an energy source and causes a jump in amplitude.

Parametric resonance occurs for drive frequencies at or near $2\omega_0/n$ where n is a positive integer [45]. When $n = 1$ and the drive frequency is at or near 2ω , it is termed *primary parametric resonance*; this first instability region is the most commonly studied and will be the focus of the remainder of this work. Parametric resonance is generally difficult to achieve for any $n > 1$ in macroscopic systems due to energy losses in the system, but can be more readily demonstrated in microsystems due to their ability to overcome damping. The first demonstration of multiple parametric resonance instabilities in a micromechanical system comes from Turner et al. in [45]. A torsional microelectromechanical resonator is driven into out-of-plane cantilevered rotation using comb drive levitation, and the first

five regions of instability are mapped and compared to theory. The authors suggest that parametric excitation in microelectromechanical systems can be used to reduce parasitic signals that sometimes cause concern in capacitive sensing, and in this particular device, increase the sensitivity of atomic force microscopy measurements. Since then, parametric resonance has been demonstrated in a wide variety of micromechanical systems for a wide variety of purposes, including mass detection with high sensitivity using microbeams [46, 47], robust micro-gyroscopes that are less sensitive to parameter variations due to their dynamical properties [48], and in bandpass filter applications [49]. An excellent review of parametric resonance in MEMS can be found in [50].

Parametric resonance can be described mathematically by the general form of the linear, undamped Mathieu equation, which is given by

$$\ddot{x} + (\delta + \epsilon \cos \omega t)x = 0 \tag{2.3}$$

where δ refers to the forcing strength and $\epsilon \cos \omega t$ is the parametric perturbation. The linear Mathieu equation can be used to describe systems undergoing external periodic forcing, and the solutions describe the boundaries of the instability zones as drawn in the $\epsilon - \delta$ parameter space [51, 52]. Readers may encounter the linear Mathieu equation in alternate forms, such as $\ddot{x} + (\delta + 2\epsilon \cos 2t)x = 0$ [35], or

$\ddot{x} + (a - 2q \cos(2\tau))x = 0$ [52], where different scaling methods lead to different forms. Those interested in a visual approach to Mathieu functions are strongly encouraged to read [53], which also nicely summarizes different vocabulary and notation used throughout literature to describe Mathieu functions.

For systems undergoing dynamics described by the Mathieu equation, the boundaries of the instability zones are a critical data set. The instability zones are the regions of drive frequency and amplitude parameter space in which parametric resonance will occur, and can be numerically determined by solving Equation 2.2.2 for the boundaries in the $a - q$ or $\delta - \epsilon$ parameter space. [35] shows the first several instability zones as determined by the linear Mathieu equation. More practically, these instability zones are mapped experimentally by varying the forcing parameters and determining when parametric resonance occurs through a method of detecting the jump to the large amplitude solution. By experimentally determining the forcing parameters that lead to parametric resonance, we are able to map a curve in the amplitude and frequency parameter space, termed the Arnold tongue [54]. Inside this region, parametric resonance will occur. A representative Arnold tongue is shown in Figure 2.3, using the forcing parameters often used in MEMS - frequency and amplitude of the voltage of the input signal. The presence of a damping terms rounds the point of this curve, increasing the threshold for parametric resonance without shifting the tongue in the amplitude-frequency

parameter space. Damping does not limit the growth inside the instability zone, but does affect the rate at which the amplitude grows [35].

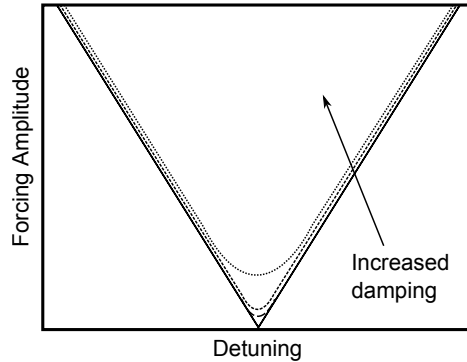


Figure 2.3: Schematic of wedge of instability for a micromechanical system. As damping increases, the threshold in the frequency-amplitude parameter space at which parametric resonance is achieved, and the point becomes rounded. A system with a higher quality factor will have a narrower tongue.

Outside the instability region, the origin is stable. Inside the tongue, the solution to the linear Mathieu equation (Equation 2.2.2) gives unbounded exponential amplitude growth. In a physical system, this unbounded amplitude would eventually lead to system failure. However, most systems possess some degree of nonlinearity that limits the amplitude, and can be more accurately represented by a nonlinear form of the Mathieu equation. The stability of the origin is the same for the linear and nonlinear systems, and so the transition boundaries are still determined using the linear Mathieu equation. Inside the tongue, the amplitude still grows exponentially, but is limited to a finite value by the nonlinearity and cannot be predicted using linear approximations. In a nonlinear system, the

system exhibits hysteresis, and the possibility of non-trivial solutions outside the instability region exists. There are many different types of nonlinearities that arise in systems described by the Mathieu equation: [55] describes a system with a quadratic nonlinearity; [47] describes a system with cubic nonlinearities; and [56] describes a system with both quadratic and cubic nonlinearities. One specific case, a microbeam subjected to periodic loading along its longitudinal axis, is described in the following section.

Case Study: Parametric resonance in a doubly-clamped beam subjected to axial loading

Here, we consider a system with a nonlinear restoring force. For the doubly-clamped beam discussed in Section 2.2.1, the stiffening cubic nonlinearity arising from the axial stretching dictates the response. The undamped nonlinear Mathieu equation with a cubic nonlinearity is given by $\ddot{x} + (a - 2q \cos 2\tau)x + a_2x^3 = u_f(\tau)$, where a_2 is the cubic stiffness coefficient, and the other coefficients retain their previous definitions.

The equation of motion describing this dynamic behavior can be rewritten using physical parameters as

$$\ddot{y} + \frac{c}{m}\dot{y} + \left(\frac{k_1}{m} - 2\lambda\omega^2 \cos(2\omega t) \frac{\pi^2}{L} \right) x + \frac{k_3}{m}y^3 = 0 \quad (2.4)$$

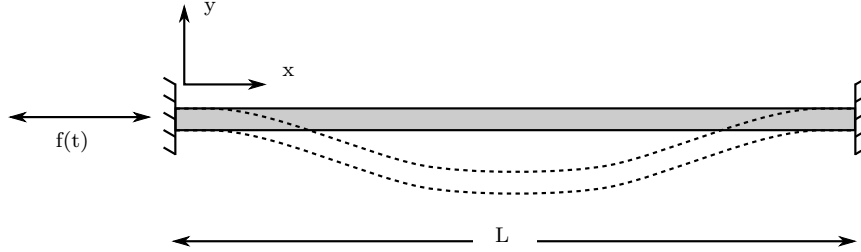


Figure 2.4: Parametric resonance in an axially-forced beam. When a microbeam is subjected to periodic loading in the axial (x) direction at twice the resonance frequency, the beam will respond with large amplitude in the transverse (y) direction at the resonance frequency. Maximum displacement occurs at $x = L/2$.

where y is the response amplitude at the center of the beam, m is the mass, c is the damping, k_1 and k_3 are the linear and cubic stiffness respectively, λ is the forcing amplitude, and L is the length of the beam. The displacement depends on the location along the beam, but in experiment, we generally refer to the maximum displacement at the center of the beam ($x = L/2$). For certain ranges of frequency and amplitude of drive, the beam will respond with large amplitude in the transverse direction. A full derivation leading to the nonlinear Mathieu equation describing the dynamics of a doubly-clamped beam can be found in [57].

In this system, the amplitude does not grow unbounded, but is limited to a finite displacement envelope by the stiffening cubic nonlinearity. At a single forcing amplitude, as we sweep frequency from left to right across the instability region, we start outside the tongue with the stable solution at the origin. As the drive

signal parameters cross the left boundary, a supercritical pitchfork bifurcation [58] occurs. The stable trivial solution becomes unstable, and two stable large amplitude solutions appear as upper and lower branches. Across the right boundary, the unstable zero solution becomes stable again. The system exhibits hysteresis, and the stable large amplitude solution continues to grow for a short time, eventually collapsing again onto the zero solution. Another unstable solution also appears.

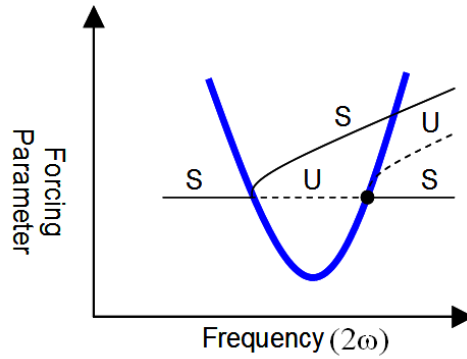


Figure 2.5: Stable and unstable solutions for primary parametric resonance instability region. At a single forcing amplitude, with increasing forcing frequency, the stable zero solution becomes unstable as the left boundary is crossed, and a stable large amplitude solution appears as a supercritical pitchfork bifurcation appears. As the right boundary is crossed, the origin becomes stable again.

At a single drive signal with frequency and amplitude parameters that fall inside the tongue, the response grows exponentially, as in the linear case, and then settles to a large amplitude solution dictated by the nonlinearity. The amplitude response of a doubly-clamped microbeam driven at 2ω with sufficient drive am-

plitude, with a cubic nonlinearity included as in Equation 2.4, is shown in Figure 2.6.

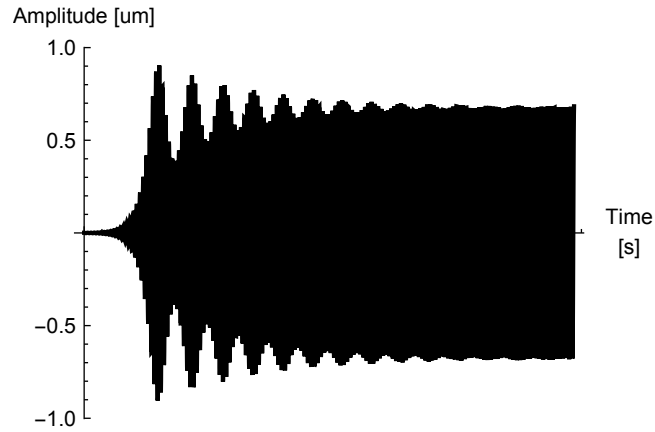


Figure 2.6: Response of a doubly-clamped beam subjected to axial loading, with $L = 500 \mu\text{m}$, $b = 20 \mu\text{m}$, $h = 1.5 \mu\text{m}$, $c = 5 \times 10^{-8} \text{Ns/m}$ and $\lambda = 6 \times 10^{-6} \text{m}$ in Equation 2.4.

In the next chapter, we'll use this discussion of parametric resonance in an axially forced beam in our development of a general model for a mechanical frequency divider that utilizes parametric resonance in coupled microbeams.

Chapter 3

Mechanical Divider Theory and Design

Invention, my dear friends, is 93% perspiration, 6% electricity, 4% evaporation, and 2% butterscotch ripple.

Willy Wonka

3.1 Subharmonic resonance cascade theory

Multiple approaches to the mechanical implementation of passive multi-stage frequency divider were explored. The first specific approach involves coupling between orthogonal microbeams with spatially localized modes, discussed in the following section. A generic model of a beam-spring mechanical implementation of a subharmonic resonance cascade is shown in Figure 3.1. A sinusoidal signal applied to u_0 at twice the frequency of the highest frequency mode (u_1), when it has sufficient amplitude to overcome losses in the system, drives u_1 into para-

metric resonance through the coupling of the spring connection. The motion in u_1 then excites parametric resonance in u_2 . This excitation continues down the chain, eventually exciting the entire cascade, due to the 2:1 frequency ratios and nonlinear coupling between modes. Eventually, the entire chain is excited, and frequency division by 2^N is achieved, where N is the number of modes. Strachan, Shaw, and Kogan present the development of the full set of equations describing the dynamics of an infinite chain in [11], which shows that for a particular scaling of nonlinearity and intermodal coupling, and above a critical forcing level, all modes will be activated and reach equal amplitude solutions.

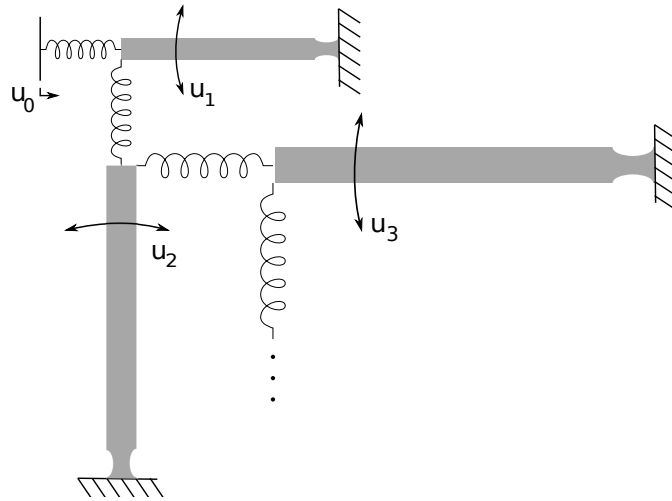


Figure 3.1: Generic model of a mechanical implementation of a resonance cascade showing the first three localized modes and coupling elements [11]. u_0 actuates the cascade of modes 1- n with degrees of freedom u_1 - u_n .

This generic model, of coupled orthogonal modes with 2:1 frequency ratios, is the one considered in the remainder of this work. But note that this is not

the only approach that can take advantage of the same autoparametric resonance effects. Though this design relies on 2:1 frequency ratios, theory predicts that parametric resonance occurs when the drive frequency is $\omega_{drive} = 2\omega_0/n$, where n is an integer ≥ 1 [45]. In general, we think of the case for $n = 1$, so that $\omega_{drive} = 2\omega_0$, but other ratios of drive frequency to response frequency can also be considered. [59] demonstrates modal coupling at a 3:1 ratio. Orthogonality is also not a requirement. Flexural beams can be placed at angles other than the 90° considered here, but orthogonality does maximize the energy transfer from one mode to the next when considering axial forcing in order to actuate large amplitude transverse displacements. In addition, it is possible to couple other types of modes together, as in the case of a flexural mode coupled to a torsional mode at a 2:1 ratio [26].

3.2 Modeling of Coupled Modes

3.2.1 Coupled Modes: Long Chain

Initial work from [11] develops the dynamics of a fully activated infinite chain of subharmonic resonators. In the model development, certain assumptions were made. Specifically, it was assumed that the cubic nonlinearity and the coupling between modes each increase by a factor of four at each successive stage. Us-

ing these assumptions and modeling the cascade as an infinite chain, the model predicts an equal amplitude solution when the entire cascade is activated.

In practice, a chain of this type comprises a finite number of resonators, and the cubic nonlinearity of each mode actually decreases with increasing beam length [60]. Mathematica (Wolfram Mathematica Student Edition, Version 10.0.0.0) can be used to show the dynamics of a generic, but more realistic physical system of a “long” chain of coupled orthogonal microbeams. This approach gives us the ability to tune individual parameters of each beam, as well as coupling, input forcing parameters, and initial conditions. With quadratic coupling of the type in [11], we assume a nonlinear equation for each beam, similar to the format in [12], with modal amplitudes, natural frequencies, quality factors, and damping coefficients denoted as x_n , ω_n , Q_n , and γ_n , respectively. The dynamics of this coupled system of a finite length are described by

$$\ddot{x}_n + \frac{\omega_n}{Q_n} \dot{x}_n + \omega_n^2 x_n + \gamma_n x_n^3 + 2\kappa_{n-1} x_{n-1} x_n + \kappa_n x_{n+1}^2 = 0 \quad (3.1)$$

where modes 1 to N provide the output signals, $x_0 = F \cos(\Omega t)$ is the applied parametric force on mode 1 with $\Omega = 2\omega_1$, and the chain is terminated with $x_{N+1} = 0$. The coupling coefficients are denoted by κ , with κ_{n-1} representing forward coupling (parametric pumping from one mode to the next), and κ_n rep-

resenting back coupling (back action from from the driven mode back to drive mode). These couplings occur between each adjacent pair of modes. We'll rewrite Equation 3.2.1 in a slightly different format, for convenience later, as

$$\ddot{x}_n + 2^{1-n}c\dot{x}_n + 2^{2(1-n)}(\omega^2x + \gamma x_n^3 + 4\kappa_f x_{n-1}x_n + \kappa_b x_{n+1}^2) = 0 \quad (3.2)$$

where c is the damping coefficient, κ_f and κ_b are the forward and back coupling coefficients, respectively, and all other variables retain their previous definitions. This reformulation uses a single parameter, scaling modal damping, coupling, and frequency parameters for modes 2- N to mode 1.

A simple time domain analysis shows sequential actuation of each member of a seven-stage cascade (a method for finding averaged equations can be found in [11]).

In this model, we've assumed exact alignment of modes, with no detuning, i.e. $\omega_n = 2\omega_{n+1}$. In addition, we reverse the assumption that the nonlinearity scales by 1:4 from one mode to the next, and instead model this scaling in a more physical manner, based on dynamics of doubly-clamped beams (Section 2.2.1) and scale the nonlinearity by 4:1 ratios. We also reverse the scaling of the coupling to match the physical architecture: each successive lower frequency mode is localized in a longer, less stiff beam, transferring a smaller amount of energy. As can be seen in

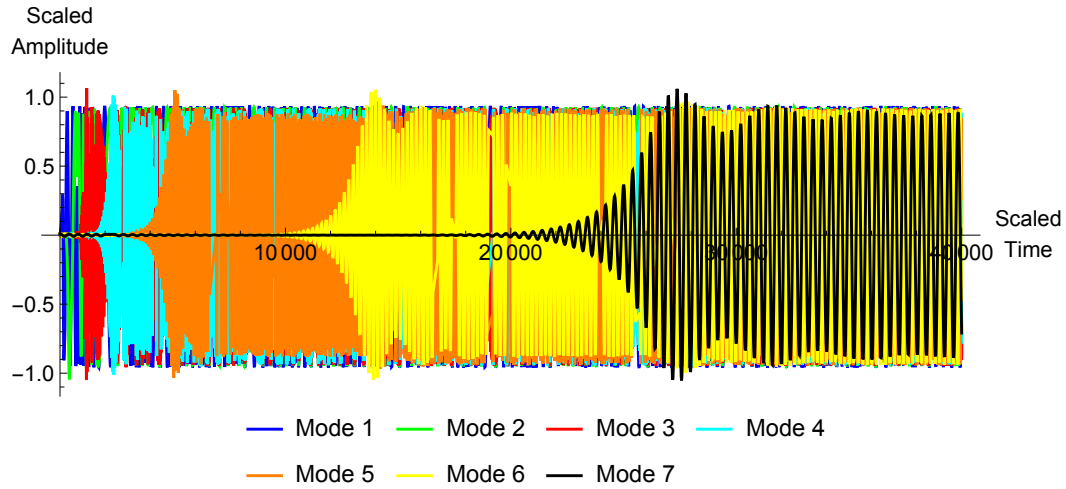


Figure 3.2: Full activation of a seven-stage cascade. Scaled system parameters from Equation 3.2.1: $F = 1$, $\gamma = .2$, $\omega = 1$, $\kappa_f = .064$, and $\kappa_b = \frac{1}{2}\kappa_f = .032$. This represents the larger of the two non-trivial solutions, with an additional trivial solution at zero amplitude.

Figure 3.2, the more realistic scaled physical system, when it reaches steady state actuation of the full cascade, just about reaches the equal amplitude solution.

Figure 3.3 shows a short segment of the time-domain response at full cascade actuation, showing more clearly the equal amplitude solution and successive frequency division by two. The last mode in the chain reaches a slightly lower amplitude, due to the fixed final boundary condition, as described in [11].

3.2.2 Two Coupled Modes

A smaller number of similarly coupled modes allows us to further investigate the complex dynamics of a subharmonic resonance cascade. Adjusting the model

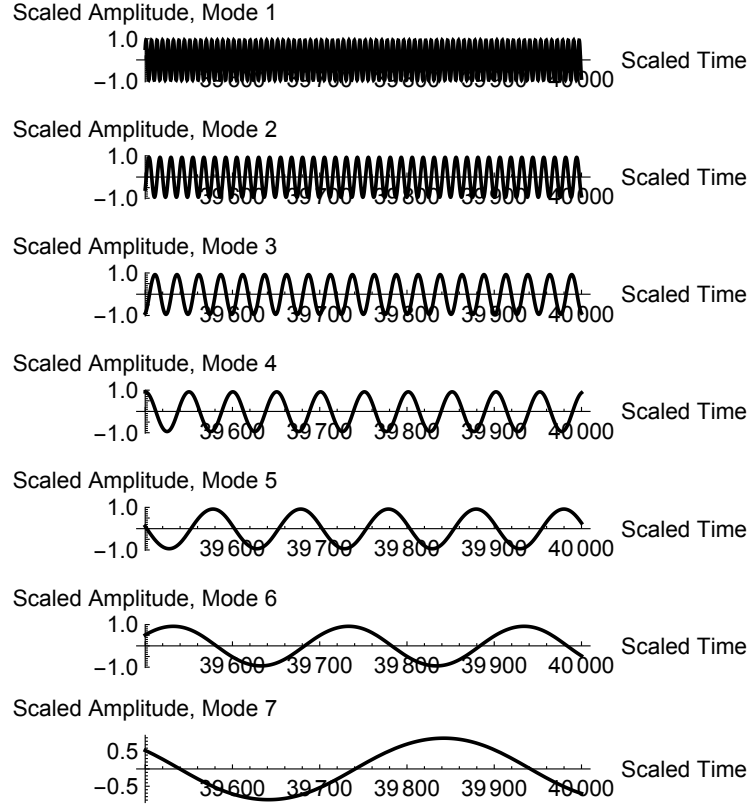


Figure 3.3: Time-domain view of full activation of a seven-stage cascade. Scaled system parameters from Equation 3.2.1: $F = 1$, $\gamma = .2$, $\omega = 1$, $\kappa_f = .064$, and $\kappa_b = \frac{1}{2}\kappa_f = .032$. Note here that the last mode has a slightly smaller amplitude, as predicted by [11], due to the fact that the last mode couples to a mode with zero amplitude, corresponding to a fixed boundary condition.

to account for smaller number of stages, and expanding to including more complex phenomena like nonlinear damping, or fabrication-related problems like detuning from physical fabrication inconsistencies, we begin to see interesting effects in the response of each mode. In the following sections, we investigate the response of two coupled modes, mode 1 and mode 2, where mode 2 has a frequency half

that of mode 1, or $\omega_1 = 2\omega_2$. Mode 1 is actuated with an input signal at $\omega_{in} = 2\omega_1$. The goal is to develop an understanding of the trends and compare them to experimental results, thereby giving us a way to recognize which effects are important and need to be included in the generic infinite chain model.

Forcing Bias

Here, we hold the amplitude of the sinusoidal input signal constant while increasing the bias. This changes the range of direct and parametric forcing in which both modes actuate. The results are shown in Figure 3.4.

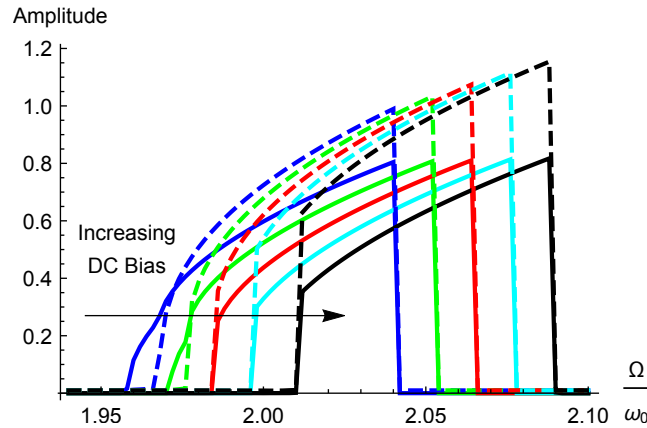


Figure 3.4: Effects of asymmetric forcing levels (DC) on response of mode 1 and 2 in a coupled two-mode system. Solid lines represent response of mode 1 and dashed lines represent the response of mode 2, with $\omega_1 = 2\omega_2$.

As expected, the increasing bias shifts the response frequencies higher. The amplitude of mode 1 also increases, while the amplitude of mode 2 remains con-

stant. An interesting result is that with increasing bias, the transition to large amplitude becomes a sharp jump. This occurs in both modes.

Nonlinear Damping

Up to this point, we have considered only linear damping. As described in [61], when the response amplitude is large enough that we need to consider nonlinear stiffness terms, like the cubic term for a single beam in Equation 2.2 or for coupled modes in Equation 3.2.1, we should also include a nonlinear damping term of the form $\zeta_{n,2}x_n^2\dot{x}_n$, which increases with amplitude, where $\zeta_{n,2}$ is the nonlinear damping coefficient. Redefining the linear damping coefficient to $\zeta_{n,1}$, where $\zeta_{n,1} = \frac{\omega_n}{Q_n}$, the equation of motion for two coupled modes can be given as

$$\ddot{x}_n + \zeta_{n,1}\dot{x}_n + \zeta_{n,2}x_n^2\dot{x}_n + \omega_n^2x + \gamma_nx_n^3 + 2\kappa_{n-1}x_{n-1}x_n + \kappa_nx_{n+1}^2 = 0 \quad (3.3)$$

Results for this system are shown in Figure 3.5.

Nonlinear damping affects the amplitude of the response. As the nonlinear damping coefficient is increased, the response of mode 1 flattens. The spikes seen at the end of the last two levels of nonlinear damping are an artifact in the model and could not be resolved within the constraints of the working memory of the computer.

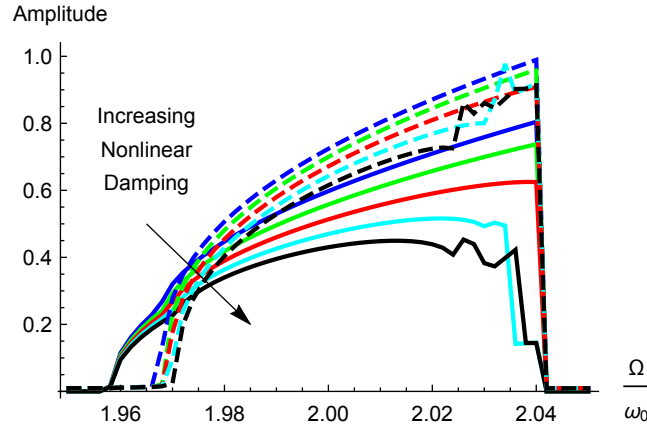
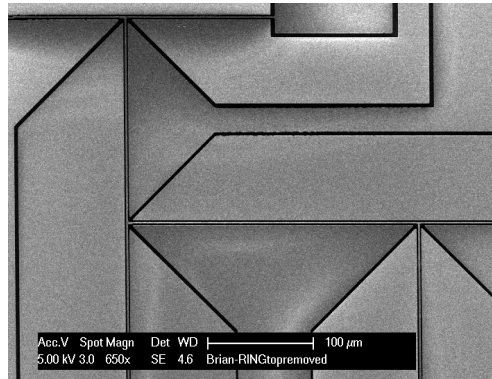


Figure 3.5: Effects of nonlinear damping on response of mode 1 and 2 in a coupled two-mode system. Solid lines represent response of mode 1 and dashed lines represent the response of mode 2, with $\omega_1 = 2\omega_2$.

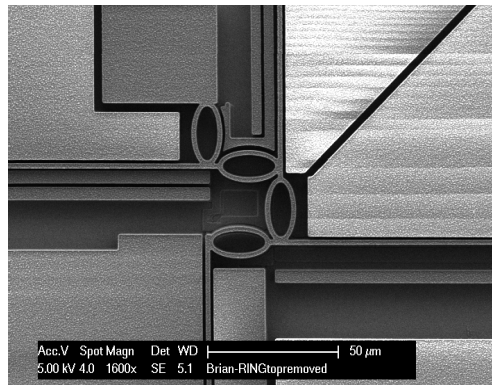
3.3 Semicircular Spring Implementation

3.3.1 Design Considerations

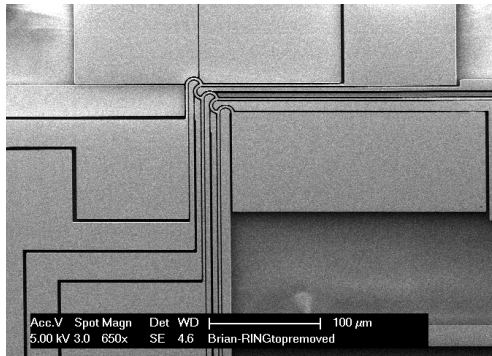
The general theory introduced in Section 3.1 describes the design of a resonance cascade of individual microbeam elements, each one sequentially perpendicular and mechanically coupled to its two nearest neighbors (Figure 3.1). The coupling in the mathematical model developed there is quadratic in nature, but makes no reference to any particular geometry. Three different coupling structures were considered. The first involves direct coupling between two nearest neighbors, shown in Figure 3.6a. The other two approaches involve springs between orthogonal beams: Figure 3.6b shows orthogonal beams connected by elliptic springs, and in Figure 3.6c, the springs are semi-circular.



(a) Directly connected



(b) Elliptical springs



(c) Semi-circular springs

Figure 3.6: Three implementations of orthogonal microbeam frequency dividers. In (a), orthogonal microbeams are fixed at both ends and directly connected to nearest neighbors at midpoints. In (b) and (c), one end of each microbeam is fixed, and spring connections are used between nearest neighbors at the other ends.

In the following sections, we discuss the design, testing, and results of a divider of the third type. In this layout, as shown in Figure 3.6c, the coupling geometry is a semicircular spring between orthogonal microbeams. Modes are spatially localized in beams 1-4, and the springs provide weak coupling between modes. The geometry is shown in Figure 3.7. An animation of how this divider works can be found at Dr. Turner's research group website [62].

We begin with the design of a four-stage cascade, with $N = 4$, though the same constraints apply to an arbitrary number of modes. Several design considerations, listed below, were used to guide the layout of the device.

1. The frequency of the fundamental mode of each stage in the cascade must be under 1 MHz. This allows us to use laser Doppler vibrometer measurements with a limit of 1.5 MHz, as well as a stroboscopic planar motion analyzer, which has a limit of 1 MHz. This does not include the frequency of the 0th beam, which is designed to be actuated at a higher frequency off resonance.
2. Each subsequent frequency must be half that of the previous mode. That is, $f_n = 2f_{n+1}$.
3. In the case of the elliptic or semicircular springs, the stiffness of the coupling structure, and by extension the coupling between modes, must be weak enough so that the modes are spatially localized in the beams, but

sufficiently strong enough to transfer energy and provide parametric pumping from one stage to the next.

4. The depth of the released structure must be significantly higher than the in-plane dimensions, in order to isolate flexural modes in plane.
5. For a simple and repeatable fabrication process consistent over a full wafer, the gap and line sizes must be able to be realized using projection lithography and deep reactive ion etching.

3.3.2 Numerical Analysis - Modal Mechanics

In our mathematical model of coupled modes in parametric resonance, we have assumed behavior similar to that of a doubly-clamped microbeam for each mode. We have included a hardening cubic stiffness term due to axial stretching, and assumed negligible higher order nonlinearities at the expected amplitudes. The microbeams of our structure, with different boundary conditions at the semi-circular spring connections, as well as coupling effects between modes, may not exhibit the same behavior. Using mechanics analysis with finite element analysis verification, we investigate the relevant terms affecting the frequency and dynamics of a single beam-spring (Figure 3.7).

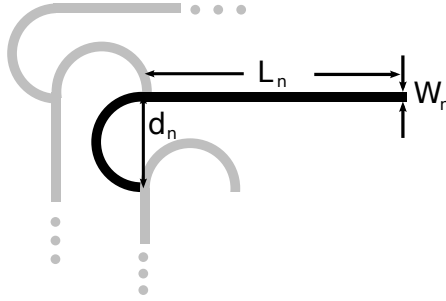


Figure 3.7: Design dimensions for a mechanical frequency divider comprising semi-circular springs with diameter d_n between orthogonal beams with length L_n and width W_n , with in-plane device depth b_n .

We first consider a doubly-clamped beam, with analytically determined linear stiffness $k_1 = 192EI/L^3$ and cubic stiffness $k_3 = 11.92EbL^3$ [60]. We compare these analytical solutions for a particular set of geometric parameters to the solutions determined using finite element analysis (described in the following section). A transverse point load is applied at the center of the beam, and the resulting force-displacement curve is fit to a polynomial (MATLAB R2014b 8.4.0.150421). As seen in Table 3.1, these values agree with theoretical calculations for a doubly-clamped beam subjected to a point load at the center, verifying our finite element method.

Using a similar process, we determine the significant terms for the stiffness of a single beam-spring. The full analytical derivation of the linear stiffness of a beam-spring can be found in Appendix A. Using this solution, as seen in Table 3.1, the linear stiffness of a clamped beam-spring is significantly lower than that

	k_1 [$\mu\text{N}/\mu\text{m}$]	k_2 [$\mu\text{N}/\mu\text{m}^2$]	k_3 [$\mu\text{N}/\mu\text{m}^3$]
Fixed Beam, Analytical	217.6	0	40.29
Fixed Beam, COMSOL	216.83	.003	39.07
Beam-Spring, Analytical	157.22	–	–
Beam-Spring, COMSOL	157.36	5.25	.37
Coupled Beam-Springs, COMSOL	159.48	1.59	.52

Table 3.1: Comparison of analytical and finite elements methods for determining stiffness of a single beam, a single beam-spring, and coupled beam-springs. Uniform depth of $10\ \mu\text{m}$, length $100\ \mu\text{m}$, width $2\ \mu\text{m}$, with hook outer diameter of $24\ \mu\text{m}$. A point load is applied at $L/2$. The Young’s modulus E is taken to be $170\ \text{GPa}$, along axis of (100) silicon wafer, with a density of $2329\ \text{kg}/\text{m}^3$.

of a doubly-clamped beam with the same geometric and material parameters. We also see the presence of a small quadratic stiffness term for a beam-spring, which is not present in the symmetric doubly-clamped beam. Though this term is small in comparison to the linear term, an accurate numerical model of a subharmonic resonance cascade with semi-circular spring connections would need to include a quadratic term. The model developed in the previous section is generic, making no reference to specific coupling geometry, and so did not include a quadratic term.

Higher order terms are negligible in these models, as was assumed in the generical model, and so additional higher order terms need to be included. The numerical model in Section 3.2 was modified to include a quadratic term. Activation of the cascade and the resulting displacements were unaffected; the only change occurred in length of the transient build up to the large displacement envelope.

With verification that a model of a single beam-spring gives us insight into the response of that same beam-spring when included in a larger coupled system, we use our derived solutions to study the effects of different device design parameters. Varying length and spring size allows us to find the combinations of the two and determine dependence of the linear stiffness k_1 on not just L but also R , starting with assumption of similar format to a doubly clamped beam. This relationship is useful at the design stage, as we attempt to align modal frequencies at 2:1 ratios. We find that the relationship of spring radius to frequency, though it follows the expectation that larger radii correspond to lower frequencies, is not linear over wide ranges of spring size. However, in the range of interest, it can be approximated as a linear relationship, with a slope that also depends on beam length (Figure 3.8): for longer beam lengths, the slope of the spring-frequency radius decreases.

We also investigate the relationship between the ratio of L_1/L_2 , with a constant total length L , and frequency. For a symmetric doubly-clamped beam, the

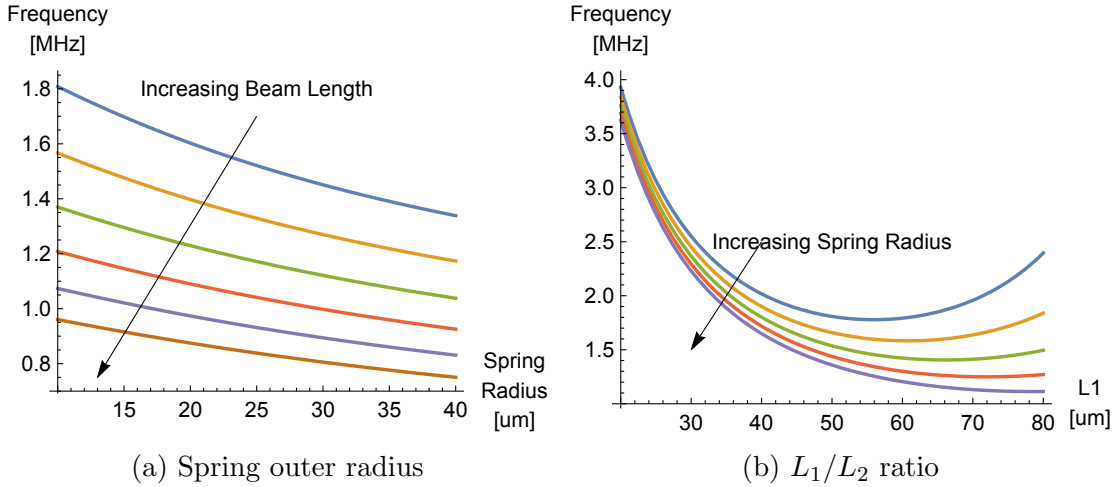


Figure 3.8: Mechanics and geometry. (a) Effects of spring outer radius on frequency, with increasing beam length L . (b) Effects of L_1/L_2 ratio with constant total beam length $L = L_1 + L_2 = 100 \mu\text{m}$ on frequency, with increasing outer spring radius.

maximum displacement occurs at the center, with $L_1 = L_2 = \frac{1}{2}L$. In the analysis of the beam-spring considered here, we have made the same assumption, but the asymmetry of the structure means that this will not be the case. We find that this relationship is highly nonlinear. As expected, for each spring radius, there is a minimum in the length ratio to frequency curve. This point is dependent on spring radius, with shorter radii corresponding to greater frequency shifts with the L_1/L_2 ratio.

This numerical analysis is useful when determining design parameters. Achieving 2:1 or very nearly 2:1 frequency ratios is successive modes is critical to the actuation of the full cascade. In addition, as we refine our design to include tuned coupling, understanding these relationships will be important.

3.3.3 Finite Element Modeling

To determine final device parameters that will align the modal frequencies in the desired 2:1 ratios, we turn to finite element analysis using COMSOL Multiphysics (Version 5.2.0.166). Though an analytical solution for the frequency of a single beam-spring was derived in the previous section, the strength of the coupling between modes in autoparametric resonance and how this coupling geometry affects the boundary conditions and frequency of each mode in the cascade is still to be determined, and so finite element analysis software is used.

Initial geometric parameters are determined by selecting a device layer depth and a uniform feature size, and then using the numerical models developed in the previous section to find the approximate length of each beam. Then, using this general layout as a starting point, finite element simulations are used to determine more exact geometric parameters of this device. The microbeam elements are chosen to be uniformly $10\ \mu\text{m}$ in depth and $1.85\ \mu\text{m}$ wide (W_n in Figure 3.7). The material properties are uniform across all microbeam elements, with E taken to be $170\ \text{GPa}$ and $\rho = 2329\ \text{kg/m}^3$. In the springs themselves, the finite element analysis takes into consideration the fact that the Young's modulus varies with θ . The beam lengths increase by approximately $\sqrt{2}$ (but not exactly) to tune the modal frequencies to decrease by a factor of 2 (Figure 3.9). Device design

parameters, determined from the COMSOL Multiphysics simulations, are shown in Table 4.1.

Note that the differing boundary conditions have significant effects on the modal frequencies. Scaling the lengths by exactly $\sqrt{2}$, as we would do for doubly-clamped beams if we wanted 2:1 ratios, and starting with $L_2 = 183.8 \mu\text{m}$, the resulting simulated frequencies are $f_2 = 419.44 \text{ kHz}$, $f_3 = 217.56 \text{ kHz}$, and $f_4 = 111.53 \text{ kHz}$, with relative intermodal frequency scaling values of 1.93:1 and 1.95:1, respectively. In order to achieve the desired 2:1 ratios between each nearest neighbor in the cascade, we must take the springs and the coupling between them into account using finite element analysis. Though each mode is spatially localized in a single beam, changing the length of a single beam affects the frequency of all other modes. This frequency shift is different for each mode, and varies with spring diameter, making analytical determination of exact frequency difficult. Note also that this is only one of many possible length specifications that achieves the desired 2:1 modal frequency ratios.

Actuation for the structure is provided through a smaller beam, termed the 0th beam, shown generically in the top left of Figure 3.1 as the drive element u_0 . The 0th beam is specifically designed not to align with the 2:1 frequency ratios. It has a much shorter length ($34 \mu\text{m}$), and so a much higher natural frequency than the highest mode in the cascade. It is actuated off-resonance using capacitive plate

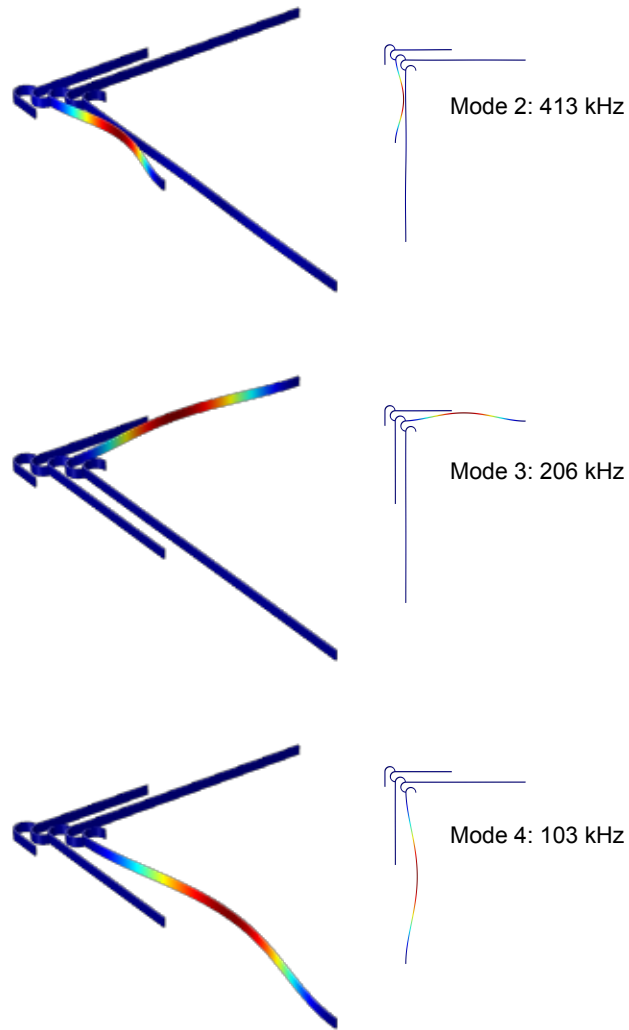


Figure 3.9: Modal analysis of three-stage divide-by-eight frequency divider. Mode 4, isolated in the longest beam, has a frequency of 103 kHz. Similarly, modes 3 and 2 have frequencies of 206 kHz and 413 kHz, respectively.

actuation, providing a force proportional to the DC and AC applied voltages, and is used to excite the resonance chain.

Chapter 4

Experimental Cascade

Invention, my dear friends, is 93% perspiration, 6%
electricity, 4% evaporation, and 2% butterscotch ripple.

Willy Wonka

4.1 Fabrication

The first successful implementation of a multi-stage passive mechanical frequency divider is shown here in a three-stage ($N = 3$) divider comprising orthogonal beams with springs between them. An SEM micrograph of the fabricated device, showing the response microbeam elements, the shorter 0th beam used for actuation, the drive electrode, and the semi-circular spring connectors, can be seen in Figure 4.1.

The released mechanical structure, spanning $400\ \mu\text{m} \times 400\ \mu\text{m}$, is fabricated in single-crystal silicon using standard SOI processing techniques. The $10\ \mu\text{m}$ device

layer on a (100) silicon wafer is patterned using projection lithography (GCA 6300 I-Line Wafer Stepper). Trenches, with the smallest at $1\ \mu\text{m}$ for the drive and sense capacitive gaps, are etched using deep reactive ion etching (Plasma-Therm 770 SLR). Wherever possible, all trenches are designed to be the same width in order to keep the etch rate consistent. Moveable structures are then released by isotropically etching the $2\ \mu\text{m}$ buried oxide layer with HF vapor (SPTS Primaxx uEtch).

4.2 Experimental Results: Divide-by-eight Cascade

The device was tested in vacuum at $350\ \text{mTorr}$ using an MMR microprobe vacuum chamber. The device is driven capacitively through the 0^{th} beam using the internal function generator integrated in the Polytec system in conjunction with an HP 3245A Universal Source for DC voltage. The velocity and phase of the in-plane motion of a point on each beam is detected using the MSA-400 Laser Doppler Vibrometer from Polytec GmbH, which uses a helium neon laser and doppler shift to measure velocity or displacement [63]. To direct the out-of-plane laser beam perpendicular to the in-plane motion, 45° angled mirrors are etched into anchored regions using focused ion beam milling [64].

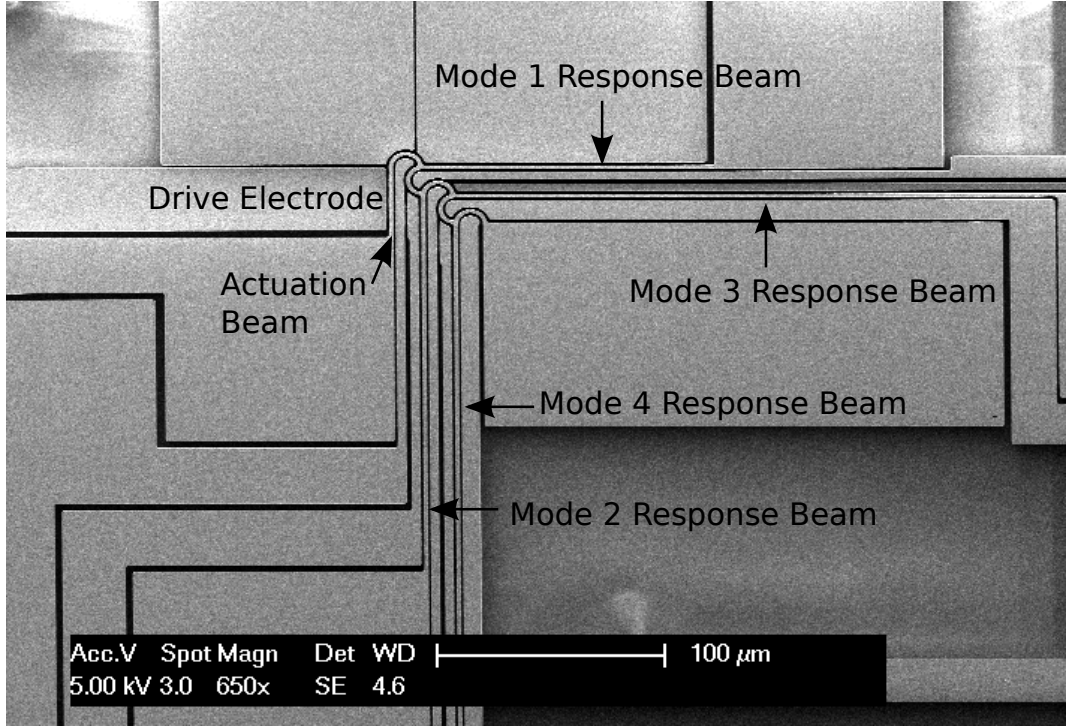


Figure 4.1: SEM micrograph of mechanical frequency divider, showing the four response beams in which the modes are localized, the shorter 0th beam and the drive electrode used for actuation, and the semicircular coupling springs. Sense electrodes are seen between the response beams, and large fixed anchors are arranged outside the device to provide surfaces to etch mirrors. The released structure is 10 μm deep with a uniform feature size of 1.85 μm . The entire device spans 400 μm x 400 μm .

The device is driven capacitively through the 0th beam at drive voltages $V_{dc} = 50\text{--}90\text{ V}$ and $V_{ac} = 3\text{--}40\text{ V}$ using the internal function generator integrated in the Polytec system. To characterize the modal frequencies, each mode is individually actuated through the 0th beam by applying $V_{in} = V_{ac} + V_{dc}$ and sweeping the frequency (ω_d) of V_{ac} . The electrostatic force f_{elec} resulting from V_{in} is given by

$$\begin{aligned}
 f_e &= \frac{1}{2}C_d(V_{ac} + V_{dc})^2 \\
 &= \frac{1}{2}C_d(V_{ac}^2\sin^2(\omega_d t) + V_{dc}^2 + 2V_{ac}V_{dc}\sin(\omega_d t))
 \end{aligned}
 \tag{4.1}$$

where C_d is the drive variable capacitance. When $V_{dc} \gg V_{ac}$, the first term in Equation 4.1 can be neglected, and the linear behavior of each beam can be characterized. A frequency sweep of the input signal with $V_{in} = 4V_{ac} + 70V_{dc}$ at the 0th beam results in a harmonic response at the modal frequencies given in Table 4.1, from which the quality factors are determined to range between 858-1315. While these measurements were taken at each individual beam, the coupling between modes allows determination of all modal frequencies at one query point.

In operation, a measurable response of mode n is observed when the amplitude of the drive signal is sufficiently large and the drive frequency is sufficiently close to $2\omega_n$. This induces a parametric resonant response in the corresponding beam, and a large amplitude solution is observed at the resonance frequency. The region of drive amplitude and frequency parameter space in which this transition occurs is determined by driving each mode independently into parametric resonance through a signal applied to the 0th beam. Due to the modal coupling in the system, each mode can be driven independently into parametric resonance without actuating the full cascade. These experimentally determined regions, termed

	Beam Length [μm]	Design Frequency [kHz]	Measured Frequency [kHz]	Quality Factor
Mode 2	183.8	420	413	1315
Mode 3	263	210	206	1035
Mode 4	376.22	105	103	858

Table 4.1: Device design parameters: beam lengths, designed and measured resonance frequencies, and measured quality factors (in vacuum), with outer hook diameter of $24\ \mu\text{m}$. Direct excitation of each mode is achieved through the actuation beam shown in Figure 4.1, with signal $V_{dc} = 90\ \text{V}$ and $V_{ac} = 3 - 10\ \text{V}$.

Arnold tongues [54], for modes 2-4 are shown in Figure 4.2. To induce parametric resonance of each mode, V_{dc} is fixed at $90\ \text{V}$ and V_{ac} is varied at twice the frequency to determine the transition between the zero stable solution and the large amplitude solution. On this particular device, the response of mode 1 was not easily observed using LDV measurements, and so actuation of the cascade begins at Mode 2.

An important characteristic of this device is the region of of drive amplitude and frequency parameter space that will cause the whole chain to be excited, thus resulting in divide-by-eight operation. To determine the region of parameter

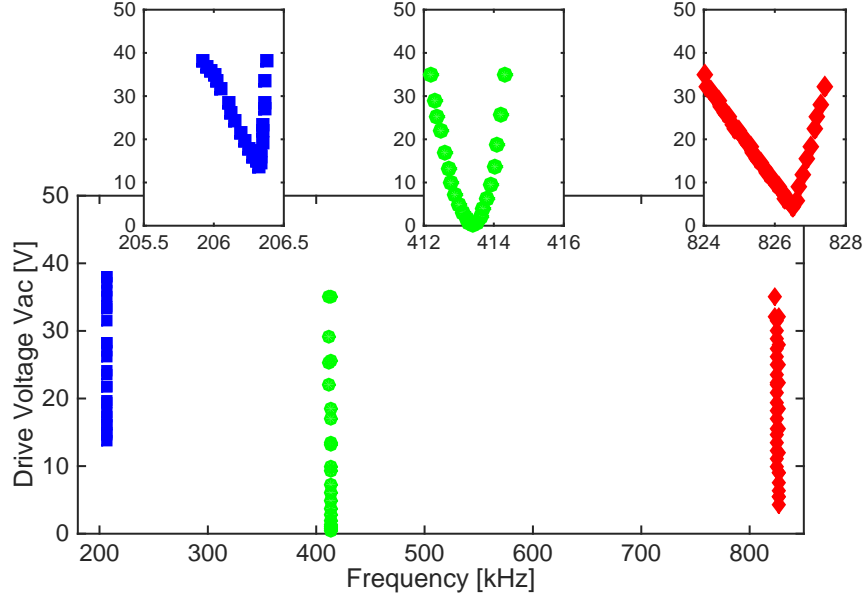


Figure 4.2: Parametric resonance zones, or Arnold tongues, for the first three modes of the device. X-axis shows drive frequency V_{ac} (ac component of drive frequency), which is at or near twice the resonant response frequency of the mode. Insets show close-ups of the tongues for clarity.

space where the entire chain of subharmonic resonances is activated, the individual Arnold tongues are normalized by mode number n and drive frequency f_{in} according to $f_{in}/(2^n f_n)$. The results of this scaling are shown in Figure 4.3. The overlap region of these three regions in this parameter space (shaded) is where the entire cascade is expected to become activated, resulting in frequency division by 2, 4 and 8. Outside of this region, some elements of the chain may be excited, depending on which region the drive amplitude and frequency fall in.

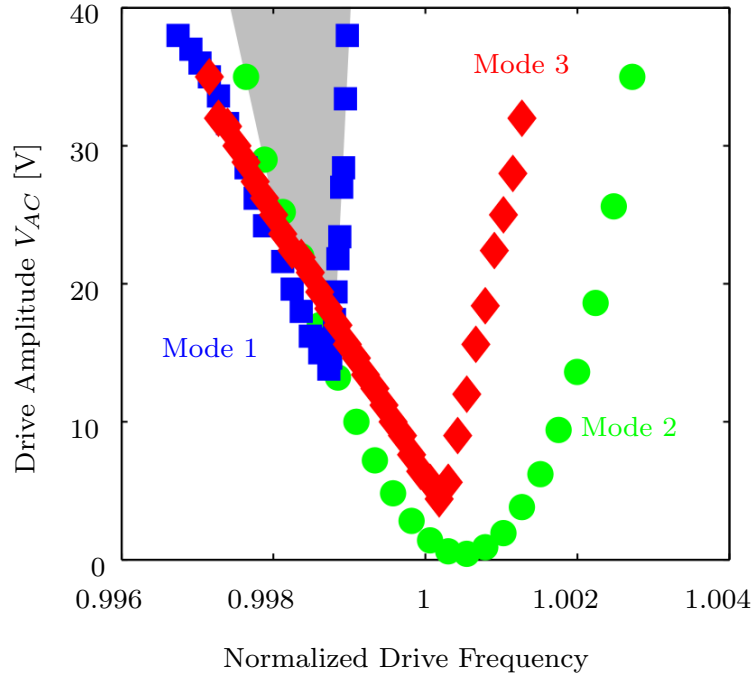


Figure 4.3: Individual tongues for modes 2-4 normalized by mode number n and drive frequency f_{in} . The overlap region (shaded) is where the divide-by-eight operation is achieved.

The instability regions observed in Figure 4.3 are not the usual single mode parametric resonance regions due to the fact that the modal responses include the dynamics of other modes. Specifically, mode n is parametrically driven by mode $n-1$, which, due to the complicated geometry, is in turn driven by both parametric and direct excitation from the drive signal. The various mode n instability wedges are dictated by these subtle effects. For example, modes 2 and 4 are parametrically driven by modes 1 and 3, respectively. Since both beams 1 and 3 are perpendicular to the drive beam, the drive signal will have a dominant parametric force and a

much smaller direct forcing term on beams 1 and 3. In contrast, mode 3 is parametrically driven by mode 2, which has a parallel orientation to the drive beam and, as a result, the drive signal has a much larger direct force on beam 2 than either beams 1 or 3. As such, the effective parametric forcing on modes 2 and 4 is considerably smaller than that on mode 3 which is why the third mode instability region is much larger than the other two instability regions.

In this device, a minimum of $19\text{ V } V_{ac}$ is required along with $V_{dc} = 90\text{ V}$ to induce a three-stage cascade with corresponding divide-by-eight frequency division using a single drive signal. At this drive amplitude, the drive frequency has a bandwidth of 400 Hz. The bandwidth of the overlap region increases to 1400 Hz with an input amplitude of $34\text{ V } V_{ac}$ with V_{dc} remaining at 90 V. This effect can be seen in Figure 4.3; as the amplitude of the drive signal increases, the bandwidth of full cascade operation grows. To demonstrate operation inside this shaded region, the 0th beam is actuated with a signal that fall inside the shaded region. A signal with an amplitude of 34 V at 824.6 kHz used to actuate the divide-by-eight cascade. The cascaded parametric response from each beam is observed and large amplitudes, obtained from the envelope of the large amplitude solution, are plotted (Figure 4.4). It is experimentally shown that large amplitudes of up to $0.7\text{ }\mu\text{m}$ are achieved using these drive amplitudes and a capacitive drive gap of $1\text{ }\mu\text{m}$ at the 0th beam.

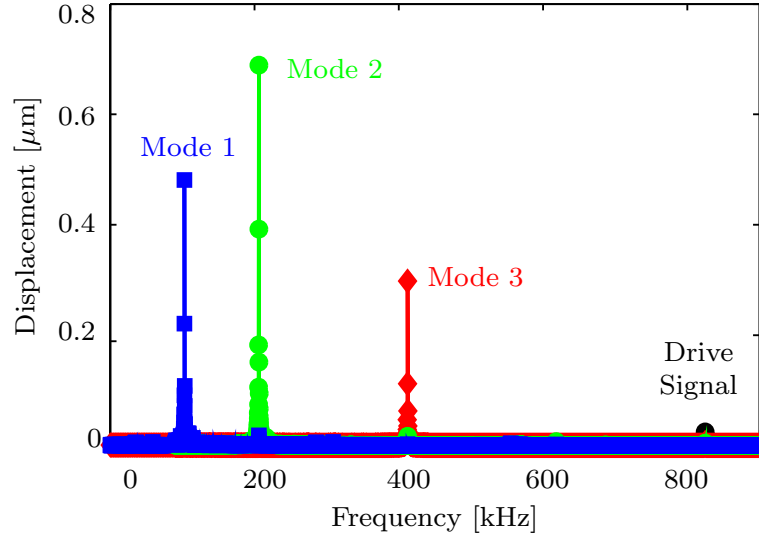


Figure 4.4: Cascaded parametric response for each mode with 824.6 kHz drive signal at $34 V_{ac}$ with a DC bias of 70 volts. Mode 2 (divide-by-two) has a gain of 12, mode 3 (divide-by-four) has a gain of 28, and mode 4 (divide-by-eight) has a gain of 20.

To show sequential activation of each mode across the different regions, we sweep frequency up across the three tongues, starting in the trivial solution zone to the left of all the tongues. Figure 4.5 shows the measured response amplitudes from modes 2-4 over the frequency range of interest indicated in Figure 4.3. When operating with a drive amplitude and frequency that falls inside all three tongues, all modes respond at the large amplitude solution. Outside of this shaded region, only one or two modes may be responding at large amplitude, depending on location inside or outside of the tongues and the direction of the sweep. Note that the mode 3 amplitude drops when mode 4 becomes active. The presence of a

mode 3 response represents passive frequency division by a factor of 4, and mode 4 represents frequency division by a factor of 8.

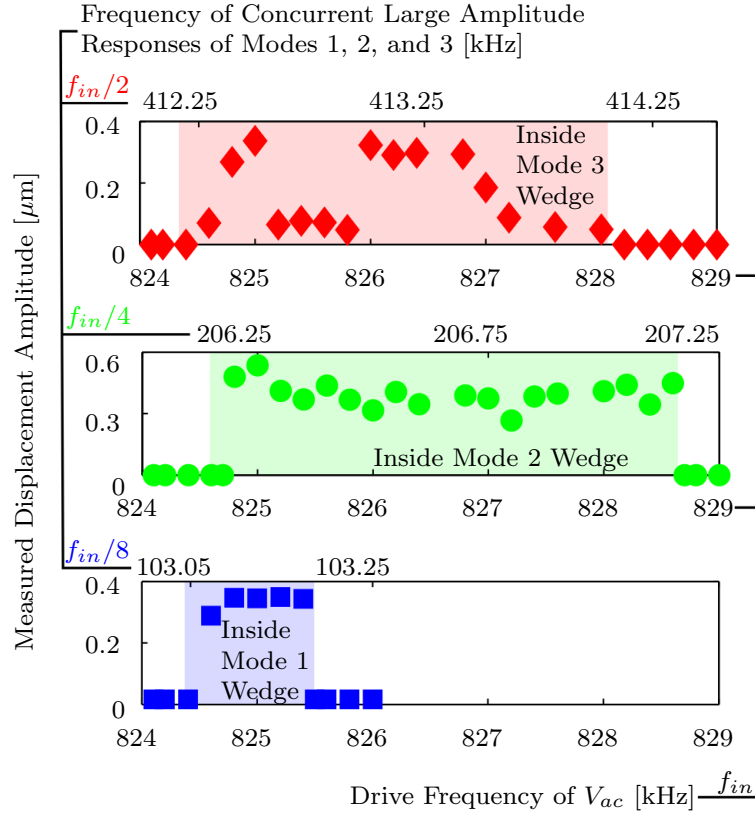


Figure 4.5: Measured amplitudes from modes 2-4, extracted from the spectrum at $\frac{1}{2}$, $\frac{1}{4}$, and $\frac{1}{8}$ of the drive frequency over the frequency range of interest; AC amplitude of 30 V. The frequency range marked with black corresponds to that of Figure 4.3, where the entire cascade activation is predicted to occur. Note that these data were taken on separate sweeps (simultaneous measurement of modes is not possible), and that the mode 4 response was slightly shifted to account for drift between the runs.

The results show successful demonstration of a multi-stage micromechanical frequency divider. A single input signal provides frequency division by two, four, a

dn eight in each of three different output elements. This proof of concept proves the capability of dividing frequency using mechanical elements and eliminating the need for noisy and high power electronic elements that are generally used to prevent back coupling. Noise characteristics of a mechanical frequency divider will be explored further in Chapter 5.

4.3 Device Characterization: Two Coupled Modes

A second device with only two coupled modes will be used to investigate the noise characteristics of this mechanical frequency divider design (Chapter 5). Here, we discuss the characterization of the two resonant modes of interest of this device; we focus on the coupling between modes 2 and 3, skipping modes 1 and 4 in the cascade. This cascade provides frequency division by two and four at the two output stages. The design, layout, and fabrication are similar to the divide-by-eight cascade in the previous section.

We use a modified experimental set up for this set of measurements in order to achieve more precise control of input parameters and data acquisition (Figure 4.6). Rather than relying on Polytec's built-in function generator, we use an external waveform generator (Agilent 33500B Series) for generating sinusoidal signals with a universal source (HP3245A) for the DC bias, and a spectrum an-

alyzer (HP89410A) to gather the data directly from the vibrometer instead of through the Polytec software interface. Chamber pressure control has also been implemented using a (MKS Type 651 Pressure Controller), allowing us to specify a set point and reach lower and more stable pressure levels. This control is done manually, and not through the computer shown in the figure.

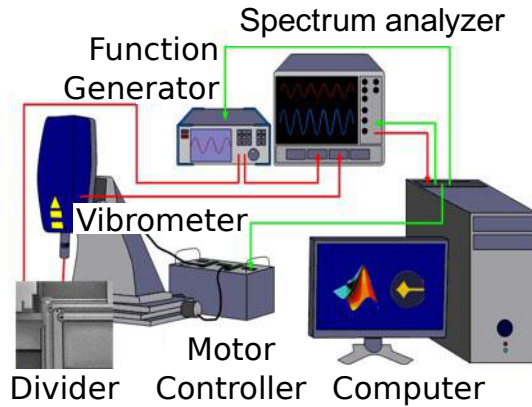


Figure 4.6: Experimental setup for velocity measurements using external components. The computer is used to control the function generator, motor controller, and gather data from the spectrum analyzer.

The method used for device actuation remains the same. The device is driven capacitively through the 0th beam and the drive electrode (Figure 4.1) at drive voltages $V_{dc} = 70\text{ V}$ and $V_{ac} = 1 - 24\text{ V}$. To characterize the linear response of modes 2 and 3, input signals at $\omega_{in} = \omega_2$ and $\omega_{in} = \omega_3$, respectively, are used. To actuate the divide-by-four cascade, the input signal at the actuation beam has a frequency of $\omega_{in} = 2\omega_2$, which actuates mode 2 and mode 3 into parametric resonance, with response frequencies of ω_2 and ω_3 .

From initial measurements, we determined frequencies of 436 kHz, 210 kHz, and 105.5 kHz for modes 2-4. Poor mirror quality prevent measurement of mode 1. Frequency ratios were determined to be 2.08:1 and 1:1.99 between adjacent modes. To align modes at the desired 2:1 ratios for cascade actuation, we begin by experimentally determining the boundaries the instability wedges in drive amplitude and frequency parameter space for each mode (Figure 4.7).

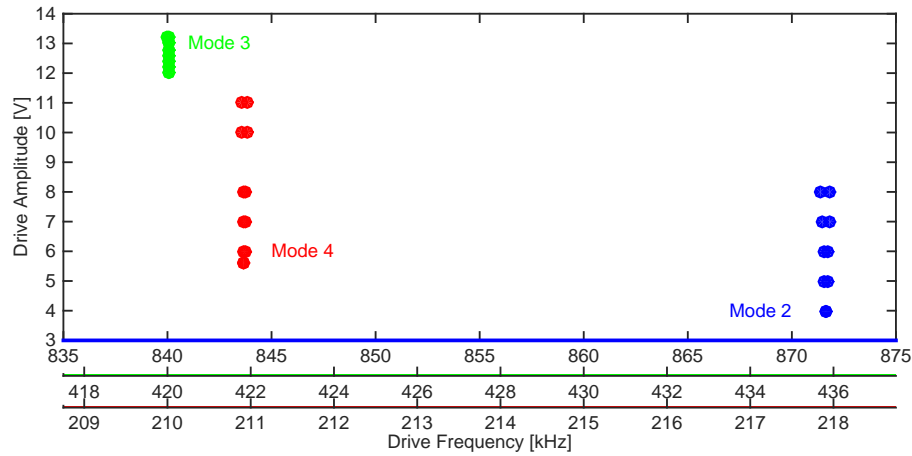


Figure 4.7: Individual tongues for modes 2-4. The drive frequency required for each mode is scaled by plotted each individually on the x-axis. Neither set of adjacent modes (mode 2 to mode 3, and mode 3 to mode 4), align at 2:1 frequency ratios. The scaled frequencies of modes 2 and 4 are too high when compared to mode 3, so the response beams in which these modes are localized will be lengthened using focused ion beam milling.

Then, focused ion beam milling was once again employed to lengthen beams in which modes that are too high in frequency are localized. Two rounds of milling were completed in order to shift the frequencies of modes 2 and 4 down. Response

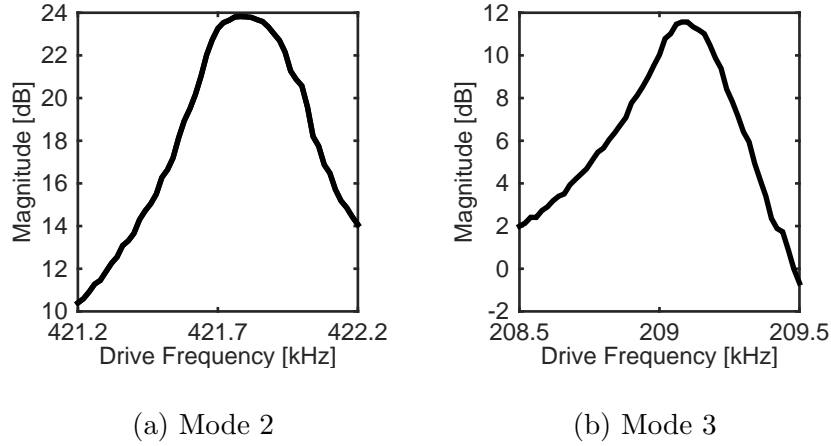


Figure 4.8: Responses of mode 2 and mode 3 to harmonic actuation. Mode 2 responds at 421.8 kHz with a quality factor of 1427, and mode 3 responds at 209.1 kHz with a quality factor of 720. This measurement was taken with a drive amplitude 6 V_{pp} at a pressure of 30 mTorr.

beams 2 and 4 were lengthened by 3.68 μm and 0.97 μm , respectively. Response beam 3 was not lengthened, as it had the lowest scaled frequency in the cascade. After this post-processing on response beams 2 and 4, mode 2 was determined to have a resonance frequency of 421.8 kHz and a quality factor of 1427, and mode 3 was determined to have a resonance frequency of 209.1 kHz with a quality factor of 720.

When the frequency sweep range for mode 3 is expanded, the amplitude-frequency response curve exhibits two peaks, one at resonance, and another about 1.5 kHz away (Figure 4.9). We believe this is due to the slight misalignment of the

frequency ratio between modes 2 and 3, as the second peak appears at $f_2/2$. This phenomenon contributes to the low quality factor, as the energy from the input voltage is distributed between generating displacement at two different frequency components. More precise alignment of sequential frequencies would eliminate this issue. As the linear drive amplitude increases, the peak at resonance increases and the second peak decreases in relative magnitude.

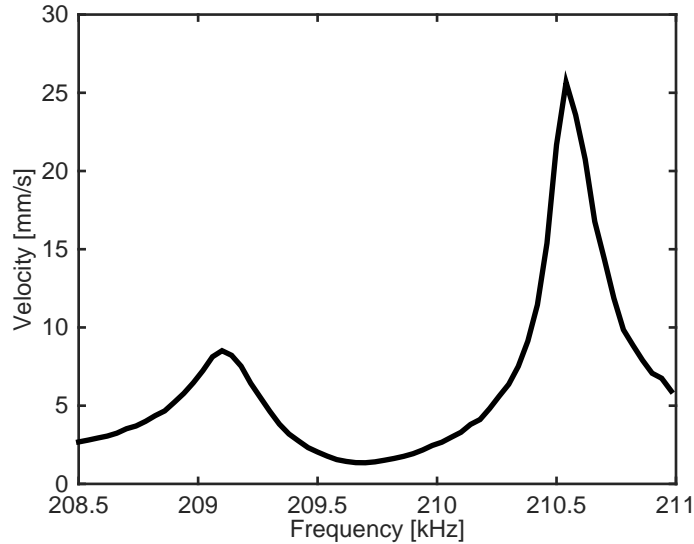


Figure 4.9: Two response peaks in mode 3. The input signal is swept near ω_3 over a wider frequency range than the measurement shown in Figure 4.8. This measurement was taken with a drive amplitude of 6 Vpp at a pressure of 30 mTorr.

The instability boundaries for modes 2 and 3 after response beam post-processing are shown together in Figure 4.10. Mode 4 did not align with the cascade, and so is not included in further discussion. A single input signal with an amplitude and frequency in the overlapping region of these tongues should be expected to actuate

the two-stage cascade with frequency divide-by-four operation. This occurs at a narrow range of drive frequencies at drive levels greater than 21 Vpp.

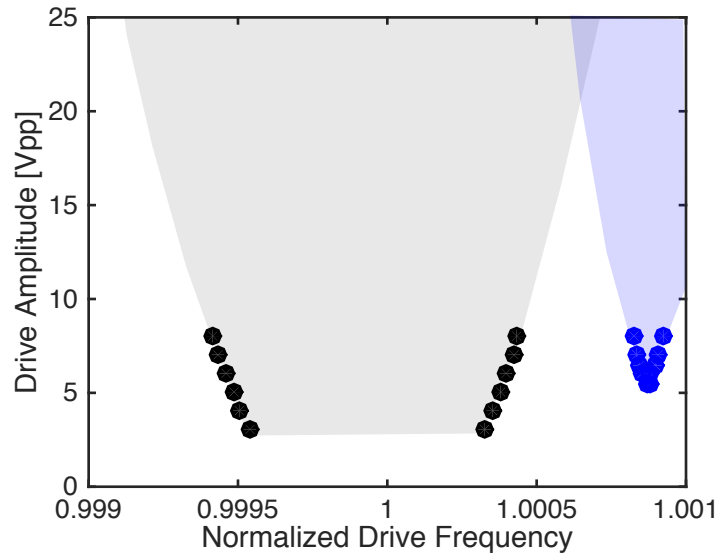


Figure 4.10: Individual instability regions after post-processing, normalized by drive frequency and mode number. The overlapping area of the two instability regions indicates the drive signal parameters that will actuate both stages of the cascade. This only occurs at drive levels above 21 Vpp.

To show sequential activation of each mode across the different regions, we sweep frequency across both instability regions tongues, starting in the trivial solution zone to the left of both tongues. Figure 4.11 shows the measured response amplitudes from modes 2 and 3 over the frequency range of interest for both forward and backward sweeps. Solid lines indicate forward sweeps, with increasing drive frequency at a given drive amplitude, and dashed lines indicated backward sweeps. As discussed in the last section, modal interactions cause the response

shape to look different than what we might expect. Here, the mode 2 response indicates a softening nonlinearity, which we do expect from a fixed microbeam. This response beam is parallel to the drive electrode, so we believe this is due to the effects of the nonlinearity caused by the strong electrostatic drive term. The mode 3 response looks more like what we would expect from a doubly-clamped beam with a hardening nonlinearity. Both modes exhibit hysteresis. Note that both modes also exhibit a plateau of displacement, similar to what we saw in the three-stage cascade (Figure 4.5). The modal interactions with bi-directional coupling limit the displacement in each mode as they transfer energy between each other.

Now that this device is characterized, in the next chapter, we will explore the effects of pressure and drive signals more in depth, with better pressure control and a new laser for better measurement capability. We will also begin to look at the noise characteristics of a parametric divider, and how noise propagates down the cascade.

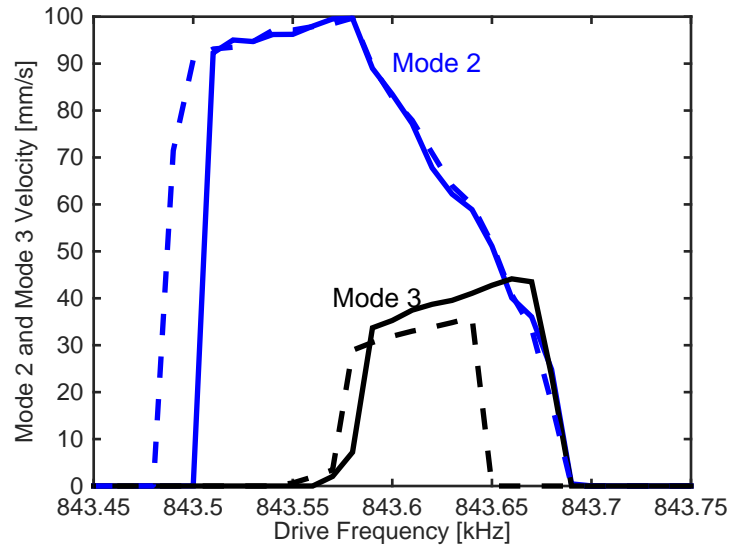


Figure 4.11: Cascade actuation using frequency sweeps across instability wedges of modes 2 and 3. Data taken at $\frac{1}{2}$ and $\frac{1}{4}$ of the input frequency. Blue lines represent mode 2, black lines represent mode 3. Solid lines indicate forward frequency sweeps, dashed lines indicated backward frequency sweep. All measurements taken at 50mTorr.

Chapter 5

Noise In A Resonance Cascade

The signal is the truth.

The noise is what distracts us from the truth.

Nate Silver

5.1 Noise in MEMS

When assessing the performance of microsystems and the accuracy of their output signals, we must accept that any signal contains small, unwanted fluctuations of both phase and amplitude. These fluctuations can be represented in a sinusoidal signal by

$$v(t) = V_0 [1 + \alpha(t)] \cos [\omega_0 t + \varphi(t)] \quad (5.1)$$

where $\alpha(t)$ and $\varphi(t)$ represent amplitude and phase fluctuations, respectively.

Though there are both phase and amplitude fluctuations, the amplitude fluctua-

tions are more readily reduced or eliminated, and the phase fluctuations are the dominant component of the overall noise [65]. Small fluctuations in the phase of a waveform can build up over time, causing large variance from the average or ideal cycle, but here we'll be discussing the short-term fluctuations that occur over very short times and remain within a half-cycle $[-\pi, \pi]$, as assumed here in this definition from [66]. *Phase noise* is the frequency domain representation of these short-term time domain instabilities, and characterizes spectral purity.

There are many sources of phase noise in a microelectromechanical system. Noise can be caused by environmental factors, including temperature, humidity in the air, and Brownian motion noise, or instabilities in the device itself, such as thermal noise or flicker noise. Powered elements in the attendant electronics, such as buffers or filters, can add noise to the circuit, and device actuation mechanisms can cause device heating during operation. Measurement techniques are yet another source: heating from LDV measurements can cause drift and noise, and instabilities can be introduced when a sensing scheme affected by small Brownian motion induced problems is used, as in the case of capacitive sensing [67, 68]. Detection noise in the measurement system can also introduce noise [69]. A thorough discussion of many possible sources of noise in MEMS can be found in [67].

There are multiple definitions of phase noise present in literature. No discussion of phase noise would be complete without first mentioning the Leeson

equation [70], which describes an oscillator’s phase noise spectrum. Leeson modified this equation from its original form to include experimentally observed phenomenon, resulting in the more commonly recognized form

$$\mathcal{L}(f_m) = 10 \log \left[\frac{1}{2} \left(\left(\frac{f_0}{2Q_l f_m} \right)^2 + 1 \right) \left(\frac{f_c}{f_m} + 1 \right) \left(\frac{FkT}{P_s} \right) \right] \quad (5.2)$$

where f_0 is the output frequency, f_m is the offset frequency from carrier, f_c is the corner frequency, Q_l is the loaded quality factor, k is Boltzmann’s constant, T is the temperature, and F is the empirically determined noise factor. In more broad terms, there are two different ways of considering phase noise. IEEE Standard 1939-2008 defines phase noise $\mathcal{L}(f)$ as one half of the one-sided spectral density of the phase fluctuations [71], while other sources define phase noise as the single sideband spectral density. [66] contains descriptions of the many terms used when talking about phase noise, a timeline of how the definition has evolved over time, and the mathematical relationships between different definitions.

As wireless technology expands and communications infrastructure grow, we place more demands on the accuracy of our systems. In the following sections, we’ll discuss how to measure open loop phase noise in a microelectromechanical system, and how to reduce it in a system by exploiting nonlinearity, by operating in parametric resonance, and through careful design.

5.1.1 Measuring Phase Noise

There are two distinct methods available in the Turner MEMS laboratory for measuring short-term stability of a resonator operating in an open loop configuration. One involves measuring the jitter using time domain signals, and the other involves looking at the single side band (SSB) spectrum of the output signal in the frequency domain. It must be made clear that in this chapter, though we refer to "phase noise," we are measuring the short term stability of a resonator in an open loop configuration, not the phase noise of an oscillator operating in closed loop.

The time domain method for analyzing the short term stability of a resonator involves looking at the output signal in the time domain, measuring the duration of a clock cycle (rising edge to rising edge), and comparing the deviation $\sigma_y(\tau)$ to the average or ideal cycle. When using this method, we must collect a long enough time sample in order to capture effects beyond the time constant of the resonator, while also staying above the minimum sampling rate as determined by the frequency. The highest frequency we can capture at a given sampling rate is determined by $f_{nyquist} = \frac{1}{2}v$ where v is the sampling rate. The Nyquist sampling theorem tells us that the frequency of measurement must be twice the highest frequency component contained in the signal or $f_{samp} \geq 2f_{sig}$. This is beyond our current laboratory capabilities (LeCroy WavePro 725Zi oscilloscope only takes

20M sample points), and so all measurements reported in this chapter are gathered using frequency domain measurements.

The frequency domain method of noise analysis involves looking directly at the frequency components of the output signal. Though there are many valid approaches, we do this by looking directly at the spectral power at the range of offset frequencies using a spectrum analyzer, and comparing this to the carrier power. Care must be taken that the phase noise of the resonator is much larger than the noise of the spectrum analyzer. For the types of devices and the measurement methods used in the Turner MEMS lab, this is generally not an issue, as the internal stability of the analyzer exceeds the noise levels seen in measurements. A discussion of the limitations of this method can be found in [66].

Successful use of a spectrum analyzer for noise analysis depends the ability to take enough sample points with a small enough resolution bandwidth (RBW). A large frequency window allows us to capture power data at frequency offsets far from the carrier, but limits the resolution of the components of the frequency spectrum. A small frequency window allows us to accurately capture a signal, but only over a very small range of frequency offsets. In addition, the larger the window, or the smaller the resolution, the longer our measurement takes. A measurement of a wide frequency range with good resolution and high enough averaging take a very long time to complete, and we run into problems with drift

in the device due to heating from prolonged operation and power from the laser, and drift in the laser head itself. Using mirrors for in-plane measurements makes for a measurement that is very sensitive to even the slightest shift in the laser spot location.

To overcome this problem and gather frequency domain data in our laboratory without purchasing a phase noise analyzer, data is collected using two spectrum analyzers simultaneously. One is set to a very small frequency window with a very small resolution bandwidth, in order to gather the close-in phase noise and accurately determine the response frequency and power. Simultaneously, another spectrum analyzer set to a large window with a much larger RBW gathers data up to a 10^5 Hz offset in order to analyze far-from-carrier noise characteristics. Phase noise is often given as the ratio of the noise power at the offset frequency to the carrier power in a 1 Hz bandwidth [72], so both measurements are normalized to a 1 Hz bandwidth. This window could be increased in order to gather data at larger offset frequencies, if needed. The large coarse window prevents us from determining an accurate carrier frequency and power, so these results are compared to the carrier signal of the narrow window with fine RBW in order to accurately determine decibels below carrier.

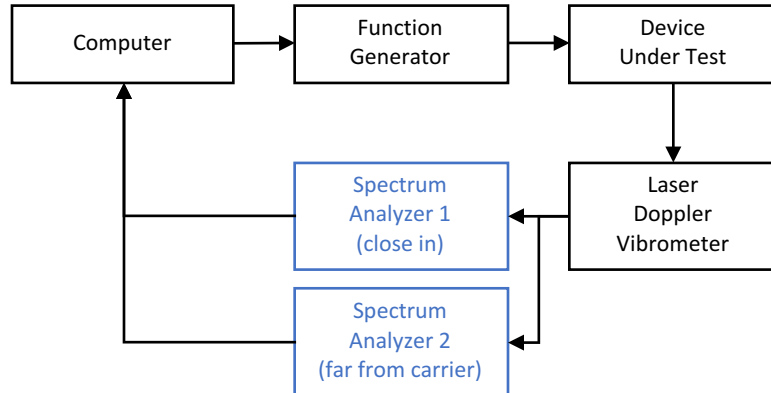


Figure 5.1: Experimental setup for measuring phase noise. Two spectrum analyzers (HP89410A) are used simultaneously to gather both close-in and far-from-carrier phase noise of the device under test from LDV measurements.

5.1.2 Reducing Phase Noise

There are many operational issues that arise when significant noise is present in a signal. Channel selectivity, important in wireless communications, can be negatively affected by phase noise when the adjacent channel power interferes with the desired signal. As the demand for available channels increases, accuracy becomes even more critical. Successful operation of tracking and guidance systems depends on a stable frequency reference [73]. Given the importance of stable signals with little fluctuation, much effort has been put into researching methods of reducing phase noise. Approaches to reducing phase noise include improving the performance of the frequency setting element itself, through careful design for high quality factor or through materials selection for long term stability, eliminating noise in the circuit elements, using filtering to improve the output signal, or using

clever design to harness the noise improvement that comes along with parametric resonance and resonator coupling.

Quartz resonators, which are often used in timing mechanisms, generally operate in the linear regime and demonstrate excellent stability characteristics. MEMS-based resonators generally lack the same intrinsic stability of quartz resonators [74], but can operate at higher frequencies, in different vibrational modes, and in the nonlinear regime, making them an attractive alternative if we can design for stability. There are several examples in literature of ways in which to exploit nonlinear phenomenon through novel design of resonator structure to improve the phase noise of MEMS resonators. Other examples of using nonlinear behavior in the resonator to improve phase noise include coupling between resonators [75], internal resonance between modes [59], parametric feedback, operating at a critical point in the nonlinear regime [76], or through appropriate feedback mechanisms. While not discussed in detail in this work, there are many other methods for improving phase noise - packaging can increase stability [77], as the environment can have a significant affect on the stability, and designing for thermal control through isolation or ovenization can improve performance [68].

Another approach involves exploiting nonlinearities or the performance enhancement of coupled resonators in arrays. Villanueva et al. show in [76] that it is possible to improve device performance by operating the resonator at special

points in the nonlinear regime and thereby reducing the phase noise below that seen in the linear regime. Using a piezoelectric doubly-clamped beam, it is shown that operation near these critical points in the $\Delta - s$ parameter space (oscillator delay and power level), termed amplitude detachment points, reduces contributions to the phase noise by phase fluctuations in the feedback and amplitude-phase conversion.

Coupled vibrational modes have been considered in many situations to improve device performance. In [59], Antonio, Zanette, and Lopez demonstrate that by coupling two vibration modes in a single nonlinear micromechanical resonator through internal resonance, the phase noise at the target frequency can be improved. Energy transfer between the first mode of a clamped-clamped beam and a higher frequency mode decreases the energy in the first mode, opposing the increase in amplitude and frequency produced by noise. Nonlinear mode-coupling was considered in [78], and a macroscale example of modal coupling based on nonlinear 1:2 internal resonance with the potential as a frequency filter-mixer or mass sensor has also been shown [79].

Replacing a single mechanical resonator element in an oscillator with an array has been shown to increase power handling and decrease phase noise [75]. In this work, a mechanically coupled free-free beam resonator array demonstrates an increased power handling ability proportional to the number of resonators in

the array and a reduction in both close-in and far-from-carrier phase noise. The far-from-carrier noise reduction is 26 dB over the input signal for an array of 10 resonators. A similar example of using an array to reduce phase noise can be found in [80], which demonstrates a phase noise reduction of 13 dB over a single resonator by using an array of nine 60 MHz wine glass resonators.

While the resonator ultimately limits the overall stability of an oscillator, electronic elements in the circuit often add a significant amount of noise. Amplifier noise evasion, as shown in [81], is a technique that exploits nonlinearity in the resonator element to suppress the noise coming from the amplifier. In a resonator with a cubic nonlinearity, using feedback at points of instability leads to stable operation throughout parameter space. In this scheme, at points of infinite slope, the frequency is insensitive to the phase of the drive, improving the noise characteristics of the resonator.

Parametric resonance, the phenomenon upon which the device in this work is based, has also been shown to improve signal quality from resonators. [82] shows that parametric amplification in a MEMS gyroscope reduces the noise associated with the desired vibrational mode with a greater than twofold increase in the signal to noise ratio. In [23], a high quality factor wine-glass disk array utilizes parametric resonance to generate a 61 MHz output signal from a 121 MHz input signal, with a 6 dB close-to-carrier phase noise reduction and a 23 dB reduction

in far from carrier noise. The 6 dB is what is expected from a divide-by-two operation, and the large reduction in the noise floor is attributed to the high quality factor of the resonator itself. [83] also uses a parametric actuation scheme to reduce phase noise. In this work, coupled nonlinear resonators are actuated above the threshold for parametric instability at specific operation points that eliminate the noise in the drive oscillator. [84] demonstrates a parametrically actuated double-clamped beam which shows improved phase noise characteristics over a traditionally operated device. The parametric feedback scheme in this work suppresses the effects of the noise in the electronics. Based on this literature, we believe that a mechanical frequency divider with nonlinear coupling between localized resonant modes in parametric resonance should demonstrate improved signal quality and higher spectral purity when compared to linear operation.

5.2 Phase noise in a cascade

As discussed in Section 5.1.2, evidence from literature suggests that the short-term stability of a particular resonance mode should improve when it is operated in parametric resonance. We measure noise characteristics of a mechanical frequency divider at each of two output stages when driven at resonance through

the actuation beam, as well as at resonance when operated in a divide-by-eight cascade in order to determine if there is any improvement in performance.

To compare the relative noise levels in two resonance modes, we start with the following equation for phase noise at an offset frequency of $\Delta\omega$, derived from equations found in [85]

$$\mathcal{L}(\Delta\omega) = 10 \log \left(\frac{2kT}{p_{sig}} \left(\frac{\omega_o}{2Q\Delta\omega} \right)^2 \right) \quad (5.3)$$

where k is Boltzmann's constant in joules/kelvin, T is the absolute temperature in kelvins, p_{sig} is the carrier power at frequency ω_0 , Q is the quality factor of the resonance mode, and $\Delta\omega$ refers to the frequency offset from carrier. Using this definition, the difference in phase noise between two modes at a certain offset frequency can be determined by

$$\Delta\mathcal{L}_\omega = 10 \log \left(\frac{\omega_1^2 p_{sig,2} Q_2^2}{\omega_2^2 p_{sig,1} Q_1^2} \right) \quad (5.4)$$

where we've assumed that $T_1 = T_2$, which we believe to be a reasonable assumption for two localized modes in the same device, tested under the same operating conditions. When modal frequencies align at 2:1 ratios, and the quality factors and carrier power signal are equal in each mode, Equation 5.4 predicts an improvement of $\Delta\mathcal{L}_\omega = 10 \log(4)$, or 6 dB, at a certain offset frequency ω for each divide-by-two operation. However, in the device considered here, the frequencies are not

perfectly aligned, and the quality factor of mode 2 is almost twice the quality factor of mode 3. Using the experimental values from Chapter 4, we can expect not an improvement, but actually an increase of over 7 dB from mode 2 to mode 3. Note that many simplifying assumptions have been made in this general model, which doesn't take into consideration the terms that were introduced by Leeson in order to match theory to experimental results, including the experimentally determined noise factor F and the modifications for the noise floor [85].

Using the frequency domain method previously described, we measure the noise characteristics of modes 2 and 3 when driven harmonically through the actuation beam in order to determine the noise characteristics in the linear regime. The open loop noise of each mode, when driven at resonance, is shown in Figure 5.2. It can easily be seen that mode 3 has a higher noise floor than mode 2 (-103 dBc/Hz and -113 dBc/Hz, respectively), and reaches the noise floor at a larger offset frequency. We can attribute this disparity in noise levels to a few factors, one of which is the relatively low quality factor of mode 3 ($Q = 720$) in comparison to mode 2 ($Q = 1427$). The nature of the frequency response of mode 3, which exhibits two peaks (Figure 4.9), is another indicator of low quality factor, and explains the two large peaks seen in the noise curve. In addition, mode 3 is closer in frequency to mode 4 than mode 2 is to mode 1, and so there is more energy

exchange between modes 3 and 4 than between modes 1 and 2 when the cascade is actuated and responding at large amplitude.

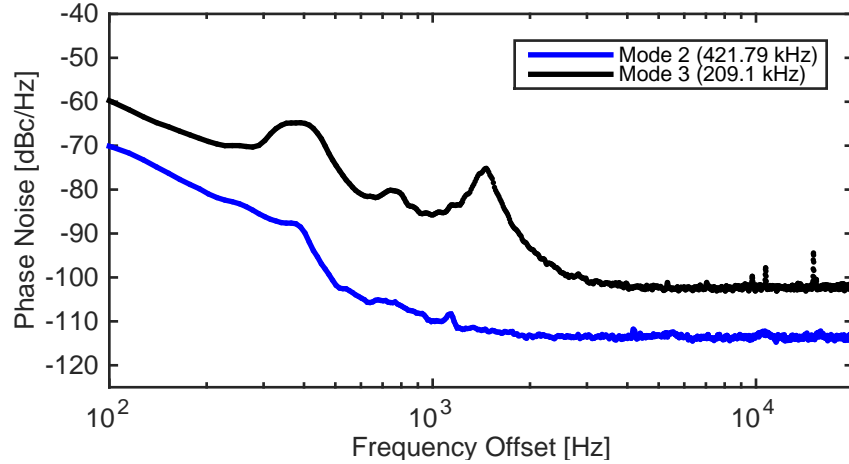


Figure 5.2: Comparison of noise characteristics of modes 2 and 3, each driven at resonance through the actuation beam. The resonance frequencies of modes 2 and 3 are 421.79 kHz and 209.1 kHz, respectively. As predicted using Equation 5.3, mode 3 shows a higher noise floor than mode 2 (-103 dBc/Hz and -113 dBc/Hz, respectively). Mode 3 also reaches the noise floor at a larger offset frequency than mode 2.

In order to investigate our hypothesis that actuating the cascade in parametric resonance will improve performance in comparison to linear operation, we drive the resonance cascade into actuation with divide-by-eight operation through the actuation beam. We use an input signal at 843.625 kHz with an amplitude of 24 V_{pp} and a 70 V DC bias, which falls inside the overlapping region of the instability wedges for modes 2 and 3. Mode 2 responds at 421.79 kHz, and mode 3 responds at 209.1 kHz. Mode 3, which when driven directly has a 10 dBc/Hz higher noise floor than mode 2, now shows improved performance, with a noise

floor equal to that of mode 2 at -113 dBc/Hz. The spurious peak seen in the linear amplitude-frequency response and in the the linear noise curve for mode 3, at an offset frequency of 1.5 kHz, has been eliminated. The close-in noise is also improved. Operating in a subharmonic resonance cascade clearly improves the quality of the response in mode 3, but only improves it to the level of what mode 2 demonstrates in linear operation.

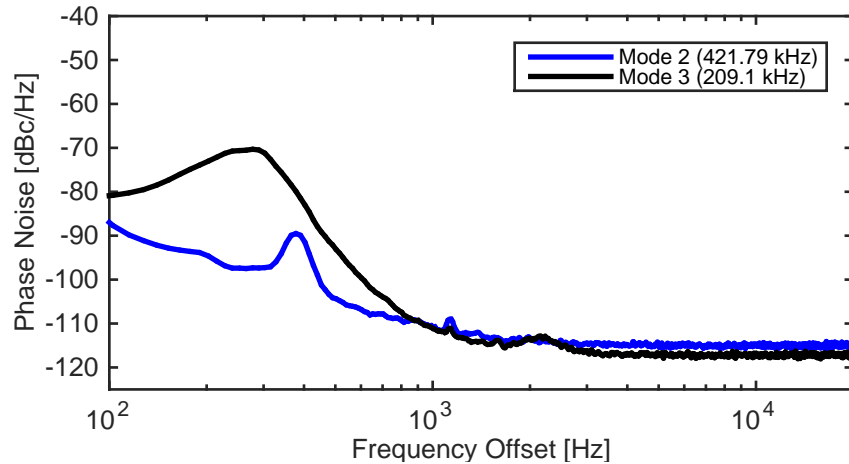


Figure 5.3: Noise in a two-stage cascade. The cascade is actuated with a drive signal at 843.625 kHz with an amplitude of 24 V_{pp} with a 70 V DC bias. Mode 2 responds at 421.79 kHz. Mode 3 responds at 209.1 kHz. Mode 3, which when driven directly has a 10 dBc/Hz higher noise floor than mode 2, now shows a much better performance. The noise in mode 3 noise has been reduced to the level of mode 2. Both modes now demonstrate equal noise floor levels at -113 dBc/Hz.

Higher quality factors could lead to even better performance. Careful redesign for more precise modal frequency alignment at $2:1$ ratios would eliminate the need for post-processing. This would significantly increase the quality factor of each mode, thereby reducing the noise in both linear and cascade operation. This

would also eliminate the spurious peaks that arise due to slight frequency misalignment. More deliberate fabrication methods for straight sidewalls and minimal undercutting at anchors would also lead to improved device performance.

An interesting investigation would be a measurement of noise in a similar two-stage cascade, where mode 3 has been designed to have a higher quality factor than mode 2. In this case, we would expect mode 3 to exhibit better noise characteristics in linear operation, and would investigate what happens to the relative noise levels when the subharmonic resonance cascade is actuated. When mode 2 has a higher quality factor, as in the experiments above, mode 3 noise is improved in the cascade. If the reverse were true, could we expect improved performance in mode 2? If a higher quality factor in mode 3 did not improve the performance of mode 2, we could say that the noise floor can only be improved to the level exhibited by the highest frequency resonator in the chain. If in fact it did improve the performance of mode 2, we could then say that we can expect noise floors in the cascade to improve to match the best performing mode in the chain. Either result would give us information on how to design for low noise resonance cascades.

We further investigate device performance by consider the effects of pressure on successful two-stage cascade actuation and corresponding noise levels. As described in Section 4.3, the device is operated in a vacuum chamber and initially

characterized at a pressure of 30 mTorr. The response of modes 2 and 3 when the divide-by-four cascade is actuated is shown in Figure 5.4 for seven different pressure levels between 30 mTorr and 150 mTorr. Four sets of data are plotted, and described here for clarity. The drive signal for two-stage cascade actuation is swept both forward and backward between 843.45 kHz and 843.8 kHz. This frequency sweep starts outside both instability boundaries, in a region where the only solution is the zero amplitude solution. As the signal over the boundaries, one or two modes may be actuated. The sweep ends in a region where only the trivial solution exists. The resulting velocity response to both forward and backward sweeps is plotted for modes 2 and 3. Mode 2 responds at $\omega_{in}/2$, from 421.73 kHz to 421.9 kHz, and mode 3 responds at $\omega_{in}/4$, from 210.86 kHz to 210.95 kHz. Solid and dashed lines denote the responses of mode 2 to forward and backward sweeps, respectively, and can be seen as a group in the top left area of the figure. Solid and dashed lines with * markers denote the responses of mode 3 to forward and backward sweeps, respectively, and can be seen in the bottom right area.

There are many interesting things to note in this plot. The response amplitude of mode 2 does not decrease significantly as the pressure level increases from 30 mTorr. In contrast, the response of mode 3 decreases significantly with increased pressure, and at approximately 130 mTorr reaches a point where the drive amplitude is no longer above the threshold for parametric resonance. This

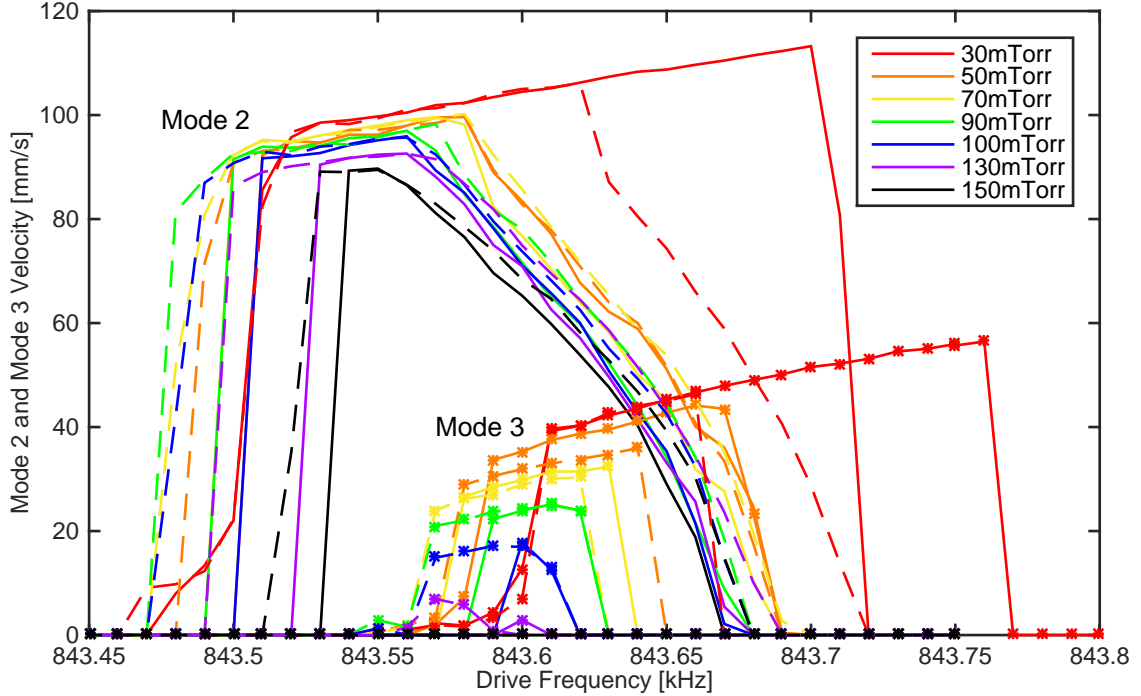


Figure 5.4: Frequency response of modes 2 and 3 at varying pressure. Four sets of data are plotted: the drive signal for cascade actuation is swept both forward and backward, and the resulting velocity response is plotted for modes 2 and 3. Solid and dashed lines indicate the response of mode 2 to forward and backward sweeps, respectively. Solid and dashed lines with * markers indicate the response of mode 3 to forward and backward sweeps. Note that the response of mode 3 decreases significantly with increased pressure, while the maximum response of mode 2 remains relatively constant.

indicates that the coupling between mode 2 to mode 3 is affected by pressure. We can also note that mode 2 exhibits signs of a softening nonlinearity. Returning to Figure 4.1, we see that the response beam in which mode 2 is localized is parallel to the electrostatic drive actuation, while the response beam in which mode 3 is localized is orthogonal to this electrostatic drive.

We then consider how the pressure level in the chamber affects the noise in each mode when driven directly, as well as at both stages when cascade is actuated. As we would expect, as pressure increases, the noise gets worse; this effect is more pronounced in mode 3. As the pressure varies from 25 mTorr up to 70 mTorr, the far-from-carrier noise floor increases in both modes when driven directly (Figure 5.5), but more so in mode 3. Mode 2 outperforms mode 3 at all pressure levels, with a lower noise floor, reached at a smaller frequency offset. At the last pressure level included in this set of measurements, 70 mTorr, both modes show a significant increase in the noise floor.

When the cascade is in operation, the pressure doesn't have nearly as much of an effect. In parametric resonance, the variability between noise floors at different pressure levels is much smaller than the variability seen in direct operation. At each pressure level, we see the same effect as in Figure 5.3, where the performance of mode 3 improves to match the performance of mode 2. Because mode 2 isn't strongly affected by pressure in the range that we are considering here, mode 3 also demonstrates less variability.

The quality of the response of each spatially localized mode in a single device is improved when operated in parametric resonance. This confirms that with further design development, we will be able to demonstrate a multi-stage mechanical

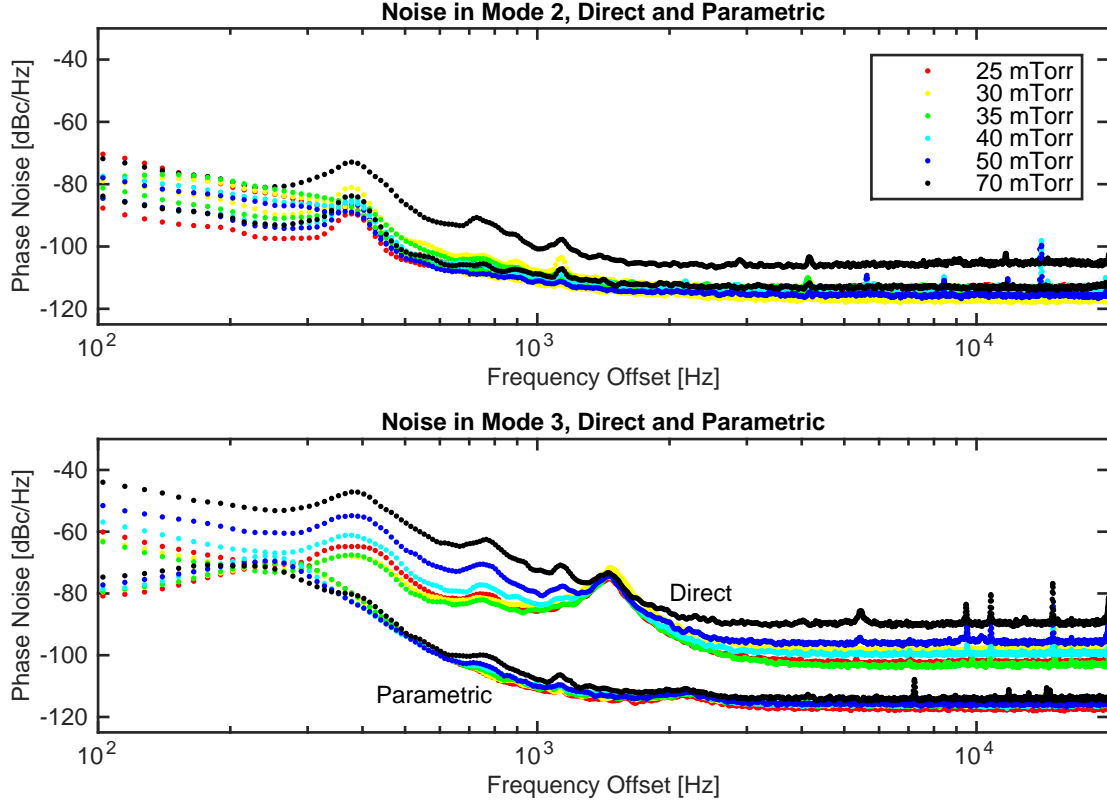


Figure 5.5: Noise at varying pressure with both direct drive of modes 2 and 3 ($\omega_{in} = \omega_2$ and $\omega_{in} = \omega_3$), and with parametric drive of mode 2 with a single signal at $\omega_{in} = 2\omega_2$ that activates the cascade. At pressures ranging from 25 mTorr to 70 mTorr, with direct drive, mode 2 always has a lower noise floor than mode 3, and reaches it at a smaller frequency offset. Both modes show poorer noise characteristics as pressure increases. In full cascade operation, the noise floor of mode 3 improves to match the performance of mode 2.

frequency divider with cascading modes that exhibit good noise quality without using powered elements.

Chapter 6

Future Work

Science never solves a problem without creating ten more.

George Bernard Shaw

6.1 Improving Performance

The goal of this work is to present a possible alternative to current electronic frequency dividers. Eliminating these electronic elements reduces the required power for operation and eliminates the noise that they add to the circuit. We have successfully demonstrated a proof-of-concept of a mechanical frequency divider that uses coupled modes and parametric resonance to divide a single input signal through several output stages.

To move beyond the proof-of-concept phase, the transition from fabrication to successful cascade operation must be improved. The process of characteriz-

ing each mode with laser Doppler vibrometry, comparing frequencies, and then post-processing the response beams is time consuming and imprecise. Most of the problems encountered during testing were due to the misalignment of modal frequencies and the low quality factor that results from milling the beams, and so a logical next step would be a redesign of the geometry based on what we've learned from testing. Characterization of multiple devices has given us a better understanding of the modal interactions and insight in to how to improve our finite element model. If we can better design for frequencies alignment during the fabrication stage, we can eliminate the need for post-processing, resulting in a streamlined design-to-device process and devices with better performance.

6.2 Device Design

Though much effort has gone into modeling and characterizing modal frequencies, at this point, there has been no effort put toward characterizing or tuning the strength of the bi-directional coupling between modes. The original mathematical model makes the assumption of forward coupling between modes scaling by 4:1 as we move down the cascade, with back coupling equal to one half of the forward coupling. Though this was not a requirement of the physical system, it does allow us to achieve an equal amplitude solution when the full cascade is actuated.

To this end, a brief investigation into the geometry of the coupling springs was performed. The current design is based on the need for the springs to be stiff enough to transmit energy, but with coupling that is weak enough to keep the modes spatially isolated. Using COMSOL Multiphysics, we investigated the coupling from the input beam to each of the output beams, as well as the coupling between nearest neighbors, as a function of spring radius. The results of varying the spring radius from $10\ \mu\text{m}$ to $14\ \mu\text{m}$ (current devices have a $12\ \mu\text{m}$ radius) indicate that increasing the spring radius increases coupling between each nearest neighbor; as expected, this effect is most pronounced from the actuation beam to the first mode in the chain. When we investigate the coupling from the actuation beam to each of the four response beams, the effect is different depending on whether the response beam is parallel or perpendicular to the actuation beam. Coupling between the actuation beam and the beams parallel to it decrease with increasing spring radius, while coupling to orthogonal beams increases with spring radius. In addition, two other coupling geometries have been fabricated, but have yet to be tested. It is possible that one of these designs has more readily tunable coupling strength. This logical next step of characterizing and tuning coupling will require further investigation.

6.3 Characterization

Laser Doppler vibrometry allows us to make incredible dynamic measurements of microstructures, determining displacement and velocity of each mode, as well as determining mode shapes and beginning to map the mechanical dynamics of interest. Currently, the Turner Lab has displacement measurement capabilities down to 0.4 pm up to a frequency of 1.2 MHz with the Polytec MSA-400, and a resolution of 1.4 pm up to 1.2 MHz with a 4 pm noise floor with the Polytec UHF-120. However, the in-plane nature of the device described in this document requires us to etch mirrors in order to direct the laser perpendicular to the motion. While the coupling between modes allows us to determine all frequencies from single measurement point, it is necessary to query each sense point individually for velocity measurements; for a device with four spatially localized response modes, this requires four etched mirrors and four separate runs of testing for one complete measurement. One drive signal is repeated multiple times, repositioning the laser spot at a different response beam each time in order to capture the dynamics. Repeated testing with varying drive parameters is time consuming and difficult, and because of the multiple runs, is prone to being affected by the environment. Another method for signal transduction would allow us to take more repeatable measurements.

A second layout of these devices was made with the intention of measuring them using capacitive sensing. An array of device geometries was made, varying the length of each response beam as well as the spring radius, in order to determine effects of geometry. Electrodes were aligned to each response beam with a 700 nm gap, in order to use capacitive parallel plate sensing at each output. This eliminates the need for mirrors, and makes it much easier to make simultaneous measurements, and makes it much easier to test multiple devices. So an array of combinations from the nominal set of dimensions was arrayed, with all possible combinations applied to three different hook sizes (18 μm , 20 μm , and 24 μm). This results in an array of 180 four-stage mechanical frequency dividers, each designed to achieve frequency divide-by-16 operation.

Actuation Beam [um]	Beam 1 [um]	Beam 2 [um]	Beam 3 [um]	Beam 4 [um]
34	130	190	272.2	390.5
		191	273.6	391
		192	275	391.5
			276.4	392
				392.5

Table 6.1: Array of dimensions in layout to determine geometric effects.

However, testing of these devices resulted in catastrophic failure every single time. As a particular mode would reach large amplitude, the response beam corresponding to that mode would pull in to the electrode. We were unable to successfully drive any of the modes into parametric resonance, and could not

characterize the cascade at a 700 nm gap size. At the larger gap size of the devices tested for the work presented here (1 μm), the change in capacitance as the beams are in motion is not detectable using equipment currently available. Capacitive sensing is a commonly used technique for signal transduction in MEMS, but for the large amplitude response of parametric resonance, other methods are used. In [86], laser Doppler vibrometry is used to sense the large amplitude displacement of a torsional MEMS resonator, but we have already seen the limitations of this method for our application. [84] utilizes two piezometallic loops fabricated on opposite sides of a MEMS cantilever, one for drive and one for sensing. There are many other examples of piezoresistive sensing in silicon-based MEMS [87, 88]. Though these approaches have proven very effective, the in-plane motion of the device described in this work makes the necessary fabrication process quite complicated.

An intriguing idea, as yet unexplored in coupled systems, is the use of magnetic fields for both actuation and sensing. In [89], axial Lorentz forces are used to drive a u-shaped cantilever into out-of-plane parametric resonance, and the resulting large amplitude displacement is sensed using magnetomotive forces. Though this was also an out-of-plane device, the sensing mechanism depends on the motion being perpendicular to the sensing field generated by an integrated permanent magnet; in-plane motion can be detected by reorienting the field. Though this

constitutes a significant redesign, it would allow rapid characterization of many devices, as we had hoped to accomplish with the capacitive sensing array.

We have demonstrated a proof-of-concept of a multi-stage frequency divider that uses mechanical coupling between resonant modes of a single structure to divide frequencies, rather than relying on noisy electronic elements in a circuit. By redesigning based on experimental results and devising a better characterization method, this concept can be developed into a repeatably realizable mechanical frequency divider for low power, low noise applications.

Bibliography

- [1] R. P. Feynman, “There’s plenty of room at the bottom,” *Engineering and science*, vol. 23, no. 5, pp. 22–36, 1960.
- [2] J. B. Angell, P. Barth, and S. C. Terry, “Silicon micromechanical devices,” *Scientific American*, vol. 248, pp. 44–55, 1983.
- [3] J. M. Bustillo, R. T. Howe, and R. S. Muller, “Surface micromachining for microelectromechanical systems,” *Proceedings of the IEEE*, vol. 86, no. 8, pp. 1552–1574, 1998.
- [4] K. E. Petersen, “Silicon as a mechanical material,” *Proceedings of the IEEE*, vol. 70, no. 5, pp. 420–457, 1982.
- [5] C. T.-C. Nguyen, “Mems technology for timing and frequency control,” in *Frequency Control Symposium and Exposition, 2005. Proceedings of the 2005 IEEE International*, pp. 11–pp, IEEE, 2005.
- [6] A. Hajimiri, “Noise in phase-locked loops,” *2001 Southwest Symposium on Mixed-Signal Design (Cat. No.01EX475)*, 2001.
- [7] H. Tilmans, W. Raedt, and E. Beyne, “MEMS for wireless communications: from RF-MEMS components to RF-MEMS-SiP,” *Journal of Micromechanics and Microengineering*, vol. 13, pp. S139–S163, 2003.
- [8] B. Razavi, “Challenges in the design of frequency synthesizers for wireless applications,” in *Custom Integrated Circuits Conference, 1997., Proceedings of the IEEE 1997*, pp. 395–402, May 1997.
- [9] F. Cottone, H. Vocca, and L. Gammaitoni, “Nonlinear energy harvesting,” *Physical Review Letters*, vol. 102, no. 8, p. 080601, 2009.
- [10] B. Williams, “Terahertz quantum-cascade lasers,” *Nature Photonics*, vol. 1, no. 9, pp. 517–525, 2007.

- [11] B. S. Strachan, S. W. Shaw, and O. Kogan, "Subharmonic Resonance Cascades in a Class of Coupled Resonators," *Journal of Computational and Non-linear Dynamics*, vol. 8, p. 041015, June 2013.
- [12] K. R. Qalandar, B. Strachan, B. Gibson, M. Sharma, A. Ma, S. W. Shaw, and K. L. Turner, "Frequency division using a micromechanical resonance cascade," *Applied Physics Letters*, vol. 105, no. 24, p. 244103, 2014.
- [13] M. M. Driscoll, "Phase noise performance of analog frequency dividers.," *IEEE transactions on ultrasonics, ferroelectrics, and frequency control*, vol. 37, pp. 295–301, 1990.
- [14] M. Tiebout, "A CMOS direct injection-locked oscillator topology as high-frequency low-power frequency divider," *IEEE Journal of Solid-State Circuits*, vol. 39, no. 7, pp. 1170–1174, 2004.
- [15] B. Razavi, K. Lee, and R. Yan, "Design of high-speed, low-power frequency dividers and phase-locked loops in deep submicron CMOS," *IEEE Journal of Solid-State Circuits*, vol. 30, no. 2, 1995.
- [16] M. Driscoll and T. Merrell, "Spectral performance of frequency multipliers and dividers," in *Frequency Control Symposium, 1992. 46th., Proceedings of the 1992 IEEE*, pp. 193–200, IEEE, 1992.
- [17] C.-M. Hsu, M. Z. Straayer, and M. H. Perrott, "A low-noise wide-bw 3.6-ghz digital fractional-n frequency synthesizer with a noise-shaping time-to-digital converter and quantization noise cancellation," *Solid-State Circuits, IEEE Journal of*, vol. 43, no. 12, pp. 2776–2786, 2008.
- [18] M. H. Perrott, S. Pamarti, E. G. Hoffman, F. S. Lee, S. Mukherjee, C. Lee, V. Tsinker, S. Perumal, B. T. Soto, N. Arumugam, *et al.*, "A low area, switched-resistor based fractional-n synthesizer applied to a mems-based programmable oscillator," *Solid-State Circuits, IEEE Journal of*, vol. 45, no. 12, pp. 2566–2581, 2010.
- [19] J. Lee and B. Razavi, "A 40-GHz frequency divider in 0.18- μm CMOS technology," *Solid-State Circuits, IEEE Journal of*, vol. 39, pp. 594–601, 2004.
- [20] B. Razavi, K. Lee, and R.-H. Yan, "A 13.4-ghz cmos frequency divider," in *Solid-State Circuits Conference, 1994. Digest of Technical Papers. 41st ISSCC., 1994 IEEE International*, pp. 176–177, Feb 1994.

- [21] H. Rategh and T. Lee, "Superharmonic injection-locked frequency dividers," *IEEE Journal of Solid-State Circuits*, vol. 34, 1999.
- [22] G. Sloan, "The modeling, analysis, and design of filter-based parametric frequency dividers," *IEEE Transactions on Microwave Theory and Techniques*, vol. 41, 1993.
- [23] T. Rocheleau, R. Liu, J. Nilchi, T. Naing, and C.-C. Nguyen, "A micromechanical parametric oscillator for frequency division and phase noise reduction," in *Micro Electro Mechanical Systems (MEMS), 2014 IEEE 27th International Conference on*, pp. 210–213, Jan 2014.
- [24] W. Lee and E. Afshari, "Distributed parametric resonator: A passive cmos frequency divider," *Solid-State Circuits, IEEE Journal of*, vol. 45, pp. 1834–1844, Sept 2010.
- [25] A. Vyas and A. Bajaj, "Nonlinear modeling of novel mems resonators," in *Proceedings of ENOC-2005: The Fifth EUROMECH Nonlinear Dynamics Conference*, 2005.
- [26] A. Vyas, D. Peroulis, and A. K. Bajaj, "Dynamics of a nonlinear microresonator based on resonantly interacting flexural-torsional modes," *Nonlinear Dynamics*, vol. 54, no. 1-2, pp. 31–52, 2008.
- [27] T. Nayfeh, W. Asrar, and A. Nayfeh, "Three-mode interactions in harmonically excited systems with quadratic nonlinearities," *Nonlinear Dynamics*, vol. 3, no. 5, pp. 385–410, 1992.
- [28] R. Lifshitz and M. Cross, "Response of parametrically driven nonlinear coupled oscillators with application to micromechanical and nanomechanical resonator arrays," *Physical Review B*, vol. 67, no. 13, p. 134302, 2003.
- [29] P. Danzl and J. Moehlis, "Weakly coupled parametrically forced oscillator networks: existence, stability, and symmetry of solutions," *Nonlinear Dynamics*, vol. 59, no. 4, pp. 661–680, 2010.
- [30] H. G. Schuster, *Reviews of Nonlinear Dynamics and Complexity*. Wiley, 2009.
- [31] M. I. Younis, *MEMS linear and nonlinear statics and dynamics*, vol. 20. Springer Science & Business Media, 2011.
- [32] G. Radons, B. Rumpf, and H. G. Schuster, *Nonlinear dynamics of nanosystems*. John Wiley & Sons, 2010.

- [33] G. Duffing, *Erzwungene Schwingungen bei veränderlicher Eigenfrequenz und ihre technische Bedeutung*. R, Vieweg & Sohn, 1918.
- [34] I. Kovacic and M. J. Brennan, *The Duffing equation: nonlinear oscillators and their behaviour*. John Wiley & Sons, 2011.
- [35] A. H. Nayfeh and D. T. Mook, *Nonlinear oscillations*. John Wiley & Sons, 2008.
- [36] B. E. DeMartini, *Development of Nonlinear and Coupled Microelectromechanical Oscillators for Sensing Applications*. PhD thesis, University of California, Santa Barbara, 2008.
- [37] J. Rhoads, *Exploring and Exploiting Resonance in Coupled and/or Nonlinear Microelectromechanical Oscillators*. PhD thesis, Michigan State University: East Lansing, 2007.
- [38] W. H. Waugh, B. Gallacher, and J. Burdess, “A high-sensitivity resonant sensor realized through the exploitation of nonlinear dynamic behaviour,” *Measurement Science and Technology*, vol. 22, no. 10, p. 105202, 2011.
- [39] H. Kauderer, *Nichtlineare mechanik: Mit 229 abb.* Springer, 1958.
- [40] A. Stephenson, *On a new type of dynamical stability*. 1908.
- [41] T. I. Fossen and H. Nijmeijer, *Parametric resonance in dynamical systems*. Springer Science & Business Media, 2011.
- [42] L. Kofman, A. Linde, and A. A. Starobinsky, “Reheating after inflation,” *Phys. Rev. Lett.*, vol. 73, pp. 3195–3198, Dec 1994.
- [43] J. Lilien and A. da Costa, “Vibration Amplitudes Caused by Parametric Excitation of Cable Stayed Structures,” *Journal of Sound and Vibration*, vol. 174, pp. 69–90, 1994.
- [44] C. C. Mei and X. Zhou, “Parametric resonance of a spherical bubble,” *Journal of Fluid Mechanics*, vol. 229, pp. 29–50, 8 1991.
- [45] K. L. Turner, S. A. Miller, P. G. Hartwell, N. C. MacDonald, S. H. Strogatz, and S. G. Adams, “Five parametric resonances in a microelectromechanical system,” *Nature*, vol. 396, pp. 149–152, 1998.

- [46] Z. Yie, M. A. Zielke, C. B. Burgner, and K. L. Turner, "Comparison of parametric and linear mass detection in the presence of detection noise," *Journal of Micromechanics and Microengineering*, vol. 21, no. 2, p. 025027, 2011.
- [47] L. Li, T. Hiller, B. Bamieh, and K. Turner, "Amplitude control of parametric resonances for mass sensing," in *SENSORS, 2014 IEEE*, pp. 198–201, Nov 2014.
- [48] L. A. Oropeza-Ramos, C. B. Burgner, and K. L. Turner, "Robust micro-rate sensor actuated by parametric resonance," *Sensors and Actuators A: Physical*, vol. 152, pp. 80–87, May 2009.
- [49] J. F. Rhoads, S. W. Shaw, K. L. Turner, and R. Baskaran, "Tunable Micro-electromechanical Filters that Exploit Parametric Resonance," 2005.
- [50] K. Moran, C. Burgner, S. Shaw, and K. Turner, "A review of parametric resonance in microelectromechanical systems," *Nonlinear Theory and Its Applications, IEICE*, vol. 4, no. 3, pp. 198–224, 2013.
- [51] L. Ng and R. Rand, "Bifurcations in a Mathieu equation with cubic nonlinearities," *Chaos, Solitons & Fractals*, vol. 14, pp. 173–181, Aug. 2002.
- [52] M. Napoli, B. Bamieh, and K. Turner, "A capacitive microcantilever: Modelling, validation, and estimation using current measurements," *Journal of dynamic systems, measurement, and control*, vol. 126, no. 2, pp. 319–326, 2004.
- [53] J. C. Gutierrez-Vega, R. M. Rodriguez-Dagnino, M. A. Meneses-Nava, and S. Chavez-Cerda, "Mathieu functions, a visual approach," *American Journal of Physics*, vol. 71, p. 233, 2003.
- [54] S. Rasband, *Chaotic Dynamics of Nonlinear Systems*. Wiley, 1997.
- [55] G. T. Abraham and A. Chatterjee, "Approximate asymptotics for a nonlinear mathieu equation using harmonic balance based averaging," *Nonlinear Dynamics*, vol. 31, no. 4, pp. 347–365, 2003.
- [56] L. Zavodney, A. Nayfeh, and N. Sanchez, "The response of a single-degree-of-freedom system with quadratic and cubic non-linearities to a principal parametric resonance," *Journal of Sound and Vibration*, vol. 129, no. 3, pp. 417–442, 1989.

- [57] Z. Yie, *Exploiting Parametric Resonance and Amplification in Microcantilever-based Mass Sensing*. PhD thesis, University of California, Santa Barbara, 2012.
- [58] S. Wiggins, *Introduction to applied nonlinear dynamical systems and chaos*, vol. 2. Springer Science & Business Media, 2003.
- [59] D. Antonio, D. H. Zanette, and D. López, “Frequency stabilization in nonlinear micromechanical oscillators,” *Nature Communications*, vol. 3, p. 806, 2012.
- [60] K. Worden and G. R. Tomlinson, *Nonlinearity in structural dynamics: detection, identification and modelling*. CRC Press, 2000.
- [61] H. G. Schuster, *Reviews of nonlinear dynamics and complexity*. Wiley Online Library, 2008.
- [62] T. M. R. Group, “Candy cane video.” <http://www.engineering.ucsb.edu/~tmems>, Accessed February 2016.
- [63] P. G. Waldbronn, “Basic principles of vibrometry.” <http://www.polytec.com/us/solutions/vibration-measurement/basic-principles-of-vibrometry/>, Accessed June 2016.
- [64] K. Turner, P. Hartwell, and N. MacDonald, “Multi-dimensional mems motion characterization using laser vibrometry,” in *IEEE Transducers 1999, Digest of Technical Papers*, pp. 1144–1147, 1999.
- [65] A. Hajimiri and T. H. Lee, “A general theory of phase noise in electrical oscillators,” *IEEE journal of solid-state circuits*, vol. 33, no. 2, pp. 179–194, 1998.
- [66] E. Rubiola, *Phase noise and frequency stability in oscillators*. Cambridge University Press, 2008.
- [67] J. Vig and Y. Kim, “Noise in microelectromechanical system resonators,” *Ultrasonics, Ferroelectrics, and Frequency Control, IEEE Transactions on*, vol. 46, pp. 1558–1565, Nov 1999.
- [68] A. Tazzoli, M. Rinaldi, and G. Piazza, “Ovenized high frequency oscillators based on aluminum nitride contour-mode mems resonators,” in *Electron Devices Meeting (IEDM), 2011 IEEE International*, pp. 20.2.1–20.2.4, Dec 2011.

- [69] Z. Yie, M. A. Zielke, C. B. Burgner, and K. L. Turner, “Comparison of parametric and linear mass detection in the presence of detection noise,” *Journal of Micromechanics and Microengineering*, vol. 21, no. 2, p. 025027, 2011.
- [70] D. Leeson, “A simple model of feedback oscillator noise spectrum,” *Proceedings of the IEEE*, vol. 54, pp. 329–330, Feb 1966.
- [71] “Ieee standard definitions of physical quantities for fundamental frequency and time metrology—random instabilities,” *IEEE Std Std 1139-2008*, pp. c1–35, Feb 2008.
- [72] X. Huang, F. Tan, W. Wei, and W. Fu, “A revisit to phase noise model of leeson,” in *2007 IEEE International Frequency Control Symposium Joint with the 21st European Frequency and Time Forum*, pp. 238–241, May 2007.
- [73] R. Sydnor, J. Caldwell, and B. Rose, “Frequency stability requirements for space communications and tracking systems,” *Proceedings of the IEEE*, vol. 54, no. 2, pp. 231–236, 1966.
- [74] M. Lutz, A. Partridge, P. Gupta, N. Buchan, E. Klaassen, J. McDonald, and K. Petersen, “Mems oscillators for high volume commercial applications,” in *TRANSDUCERS 2007-2007 International Solid-State Sensors, Actuators and Microsystems Conference*, pp. 49–52, IEEE, 2007.
- [75] S. Lee and C.-C. Nguyen, “Mechanically-coupled micromechanical resonator arrays for improved phase noise,” in *Frequency Control Symposium and Exposition, 2004. Proceedings of the 2004 IEEE International*, pp. 144–150, Aug 2004.
- [76] L. G. Villanueva, E. Kenig, R. B. Karabalin, M. H. Matheny, R. Lifshitz, M. C. Cross, and M. L. Roukes, “Surpassing Fundamental Limits of Oscillators Using Nonlinear Resonators,” *Physical Review Letters*, vol. 110, p. 177208, Apr. 2013.
- [77] B. Kim, R. N. Candler, M. A. Hopcroft, M. Agarwal, W.-T. Park, and T. W. Kenny, “Frequency stability of wafer-scale film encapsulated silicon based mems resonators,” *Sensors and Actuators A: Physical*, vol. 136, no. 1, pp. 125–131, 2007.
- [78] M. Matheny, L. Villanueva, R. Karabalin, J. Sader, and M. Roukes, “Nonlinear mode-coupling in nanomechanical systems,” *Nano Letters*, vol. 13, no. 4, pp. 1622–1626, 2013.

- [79] A. Vyas, D. Peroulis, and A. Bajaj, "A microresonator design based on nonlinear 1: 2 internal resonance in flexural structural modes," *Journal of Microelectromechanical Systems*, vol. 18, no. 3, pp. 744–762, 2009.
- [80] Y.-W. Lin, S.-S. Li, Z. Ren, and C.-C. Nguyen, "Low phase noise array-composite micromechanical wine-glass disk oscillator," in *Electron Devices Meeting, 2005. IEDM Technical Digest. IEEE International*, pp. 4 pp.–281, Dec 2005.
- [81] D. S. Greywall, B. Yurke, P. A. Busch, A. N. Pargellis, and R. L. Willett, "Evading amplifier noise in nonlinear oscillators," *Physical Review Letters*, vol. 72, pp. 2992–2995, 1994.
- [82] M. Sharma, E. H. Sarraf, R. Baskaran, and E. Cretu, "Parametric resonance: Amplification and damping in mems gyroscopes," *Sensors and Actuators A: Physical*, vol. 177, pp. 79–86, 2012.
- [83] E. Kenig, M. C. Cross, R. Lifshitz, R. B. Karabalin, L. G. Villanueva, M. H. Matheny, and M. L. Roukes, "Passive phase noise cancellation scheme," *Phys. Rev. Lett.*, vol. 108, p. 264102, Jun 2012.
- [84] L. G. Villanueva, R. B. Karabalin, M. H. Matheny, E. Kenig, M. C. Cross, and M. L. Roukes, "A nanoscale parametric feedback oscillator," *Nano letters*, vol. 11, no. 11, pp. 5054–5059, 2011.
- [85] T. H. Lee and A. Hajimiri, "Oscillator phase noise: a tutorial," *IEEE journal of solid-state circuits*, vol. 35, no. 3, pp. 326–336, 2000.
- [86] R. Baskaran and K. L. Turner, "Mechanical domain coupled mode parametric resonance and amplification in a torsional mode micro electro mechanical oscillator," *Journal of Micromechanics and Microengineering*, vol. 13, no. 5, p. 701, 2003.
- [87] S. M. Firdaus, I. A. Azid, O. Sidek, K. Ibrahim, and M. Hussien, "Enhancing the sensitivity of a mass-based piezoresistive micro-electro-mechanical systems cantilever sensor," *IET Micro Nano Letters*, vol. 5, pp. 85–90, April 2010.
- [88] B. W. Chui, T. D. Stowe, Y. S. Ju, K. E. Goodson, T. W. Kenny, H. J. Mamin, B. D. Terris, R. P. Ried, and D. Rugar, "Low-stiffness silicon cantilevers with integrated heaters and piezoresistive sensors for high-density afm thermomechanical data storage," *Journal of Microelectromechanical Systems*, vol. 7, pp. 69–78, Mar 1998.

Bibliography

- [89] M. V. Requa and K. L. Turner, “Electromechanically driven and sensed parametric resonance in silicon microcantilevers,” *Applied Physics Letters*, vol. 88, no. 26, p. 263508, 2006.

Appendices

Appendix A

Beam-Spring Stiffness

Much of the analysis of the frequency divider presented in this document assumes that each mode is that of the lowest flexural mode of a doubly-clamped beam, ignoring the spring boundary condition on one end. Here, we consider the spring and derive the stiffness of a single beam-spring subjected to a point load at the point of maximum deflection. It is tempting to consider bending only, while ignoring transverse shear and axial strain. This approximation is common, and generally only leads to a small error. However, in this case, the approximation leads to a nearly 15% error, and so all terms must be included.

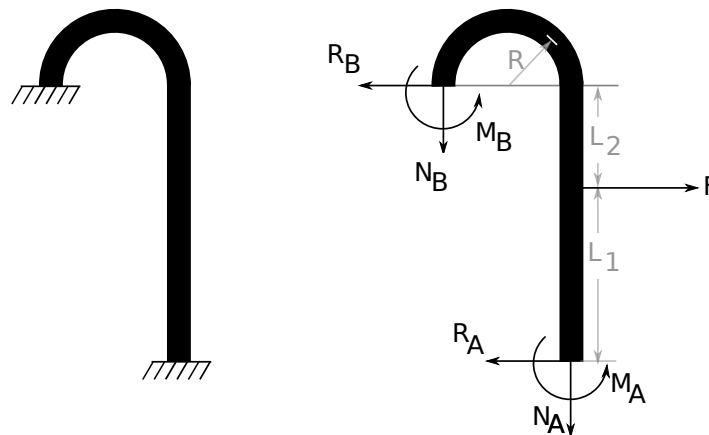


Figure A.1: Free body diagram of a single beam-spring for determining stiffness and deflection.

Finite element analysis shows that the point of maximum deflection is not at the exact center, so we use L_1 and L_2 independently. With six unknowns, this is

a statically indeterminate problem. We assume linearity and use Castigliano's second theorem, given as

$$q_i = \frac{\partial U}{\partial Q_i} \quad (\text{A.1})$$

where q_i refers to the generalized displacement, Q_i is the generalized force, and U is the strain energy. We begin by determining the strain energy due to bending (M_i), transverse shear (V_i), and tension (N_i).

$$\begin{aligned} U &= \int_0^{L_1} \left(\frac{M_1^2}{2EI} + \frac{V_1^2}{2GA} + \frac{N_1^2}{2EA} \right) dx \\ &+ \int_{L_1}^{L_1+L_2} \left(\frac{M_2^2}{2EI} + \frac{V_2^2}{2GA} + \frac{N_2^2}{2EA} \right) dx \\ &+ \int_0^\pi \left(\frac{M_3^2}{2EI} + \frac{V_3^2}{2GA} + \frac{N_3^2}{2EA} \right) R d\theta \end{aligned} \quad (\text{A.2})$$

Partial derivatives of the strain energy are used to find the reaction forces M_A and R_A .

$$\begin{aligned} \theta_A = 0 &= \frac{\partial U}{\partial M_A} \\ \delta_{x,A} = 0 &= \frac{\partial U}{\partial R_{x,A}} \\ \delta_{y,A} = 0 &= \frac{\partial U}{\partial N_A} \\ \theta_B = 0 &= \frac{\partial U}{\partial M_B} \\ \delta_{x,B} = 0 &= \frac{\partial U}{\partial R_{x,B}} \\ \delta_{y,B} = 0 &= \frac{\partial U}{\partial N_B} \end{aligned} \quad (\text{A.3})$$

We use these results to solve for the deflection at the point of application of the force F using $\delta_{x,F} = \frac{\partial U}{\partial F}$. The deflection allows us to find the linear stiffness of the structure.

Appendix A. Beam-Spring Stiffness

$$\begin{aligned}
k_1 = & 192AEGI \left[6(3\pi^2 - 16) A^2 G^2 LR^6 + 6\pi(\pi^2 - 8) A^2 G^2 R^7 + \pi i L^2 R (AGL^2(E + 9G) + 12i(e^2 + 4EG + G^2)) \right. \\
& + 3\pi R^3 (AGL^2 (AGL^2 + 20EI + 12GI) + 2\pi^2 I^2 (E + G)^2) + 12\pi AGR^5 (2AGL^2 + \pi^2 I(E + G) - 4I(E + G)) \\
& + 4AGLR^4 (\pi^2 (AGL^2 + 9I(E + G)) - 24GI) + 2ILR^2 (2AGL^2 (\pi^2 (E + G) + 12G) + 9\pi^2 I(E + G)^2) \\
& \left. + 2GIL^3 (AGL^2 + 12EI) \right] \\
\div L & \left[\pi IL^2 R (A^2 G^2 L^4 (E + 15G) + 60AGIL^2 (E^2 + 10EG + G^2) + 576EI^2 (E^2 + 5EG + 2G^2)) \right. \\
& + AGLR^4 (\pi^2 (7A^2 G^2 L^4 + 72AGIL^2 (5E + 3G) + 576EI^2 (5E + 6G)) - 768GI (AGL^2 + 12EI)) \\
& + 3\pi R^3 (AGL^2 (A^2 G^2 L^4 + 4AGIL^2 (21E + 11G) + 192EI^2 (6E + 5G)) + 16\pi^2 I^2 (E + G)^2 (AGL^2 + 12EI)) \\
& + ILR^2 (\pi^2 (E + G) (7A^2 G^2 L^4 + 18AGIL^2 (15E + 7G) + 576EI^2 (2E + 3G)) + 144AG^2 L^2 (AGL^2 + 24EI)) \\
& + 48\pi (\pi^2 - 8) A^2 G^2 R^7 (AGL^2 + 12EI) + 6(3\pi^2 - 16) A^2 G^2 LR^6 (5AGL^2 + 96EI) \\
& + 24\pi AGR^5 (4EGI ((14 + \pi^2) AL^2 + 12(\pi^2 - 4) I) + AG^2 L^2 (3AL^2 + 4(\pi^2 - 4) I) + 48(\pi^2 - 4) E^2 I^2) \\
& \left. + 2GIL^3 (AGL^2 + 12EI) (AGL^2 + 48EI) \right] \tag{A.4}
\end{aligned}$$

If we make the assumption that the point load is in the middle of the beam, $L_1 = L_2 = L/2$, and ignore shear and tension ($V_i = 0$ and $N_i = 0$), Equation A.4 reduces to the stiffness of a doubly-clamped beam, $k_1 = 192EI/L^3$ in the case of $R = 0$.